A Warm Rain Latent Heating Algorithm for CloudSat

Author:

Ethan L. Nelson

Supervisor:

Dr. Tristan S. L'Ecuyer

A thesis submitted in partial fulfillment of

the requirements for the degree of

Master of Science

(Atmospheric and Oceanic Sciences)

at the

University of Wisconsin-Madison

December 2014

Thesis Declaration and Approval

I, Ethan L. Nelson, declare that this thesis titled 'A Warm Rain Latent Heating Algorithm for CloudSat' and the work presented in it are my own.

Ethan L. Nelson		
Author	Signature	Date

I hereby approve and recommend for acceptance this work in partial fulfillment of the requirements for the degree of Master of Science:

Tristan S. L'Ecuyer		
Committee Chair	Signature	Date
Gregory J. Tripoli		
Faculty Member	Signature	Date
Larissa E. Back		
Faculty Member	Signature	Date

Abstract

A Warm Rain Latent Heating Algorithm for CloudSat

by Ethan L. Nelson

Latent heating is an important process that contributes to the atmospheric general circulation. To better observe latent heating occurring globally, an algorithm is constructed for use with CloudSat using cloud resolving model simulations initially of shallow convection. Taking key characteristics of the reflectivity profile's vertical extent and intensity, a Bayesian framework calculates latent heating, surface rainfall rate, and liquid water path with associated uncertainties for the given profile. Examined first in a synthetic framework, the parameters provide sufficient information to constrain these quantities. Application to field campaign and CloudSat data yields retrievals that align with physical expectations. Having shown that the algorithm works, future plans for expansion of the algorithm to all precipitation regimes, as well as application to specific climate features, is discussed.

"He named it Ebenezer, saying, 'Thus far the Lord has helped us.'"

-1 Samuel 7:12 (NIV)

Acknowledgements

First, I would like to thank my advisor, Tristan L'Ecuyer, whose mentoring and support made this project possible. His patience and insight have been immensely helpful, and completing this work with him has transformed me into a better scientist and researcher. Norm Wood has provided invaluable assistance with program execution and model configurations for this study.

Thanks must also go to Susan van den Heever and members of her research group (Steve Saleeby, Steve Herbener, and Wesley Berg) at Colorado State University for collaborating on this project and providing the RAMS simulations. Her group served as a point of information for many of the project parts, and their help is appreciated.

My research group colleagues and friends have provided great company and help through the past few years of classes, research, life, and cheese escapades. The community at Asbury Church has also been invaluable to me during my time in Madison.

And, finally, but not least important, thanks must go to my family. Their love and support have been so helpful and they have provided the means necessary for me to be where I am right now.

Acknowledgement is made to the CloudSat Data Processing Center for CloudSat data and to Larry Oolman and David Leon at the University of Wyoming for the VOCALS-Regional Experiment C-130 radar data.

This work was supported by the NASA CloudSat/CALIPSO Science Team under Grant #NNX12AC51G and by NASA Headquarters under the NASA Earth and Space Science Fellowship Program under Grant #NNX14AL35H.

Contents

List of Figures

List of Tables

Abbreviations

ATEX	**A**tlantic **T**rade Wind **Ex**periment
cc	number concentration per **c**ubic **c**entimeter
CCNC	**c**loud **c**ondensation **n**uclei **c**oncentration
CPR	**C**loud **P**rofiling **R**adar (aboard CloudSat)
CRM	**c**loud **r**esolving **m**odel
dBZ	**d**eci**b**els relative to radar reflectivity
GHz	**g**iga**h**ert**z**
K	**K**elvin
m	**m**eter
MJO	**M**adden-**J**ulian Oscillation
NASA	**N**ational **A**eronautics and **S**pace **A**dministration
PIA	**p**ath **i**ntegrated **a**ttenuation
PIR	**p**ath **i**ntegrated **r**eflectivity
PR	**P**recipitation **R**adar (aboard TRMM)
RAMS	**R**egional **A**tmospheric **M**odeling **S**ystem
RMSE	**r**oot **m**ean **s**quare **e**rror
TRMM	**T**ropical **R**ainfall **M**easuring **M**ission
SST	**s**ea **s**urface **t**emperature
VOCALS	**V**AMOS **O**cean **C**limate **A**tmosphere and **L**and **S**tudy

Chapter 1

Introduction

1.1 Preface

The observation and study of latent heating has a long history outside of the atmospheric sciences. More recently, the effects of latent heating on the atmosphere and ocean systems have been explored in-depth from mesoscale to climatic orders of time length. Because of the inability to directly measure latent heating, other atmospheric properties must be utilized to quantify this phenomenon. An approach to constraining latent heating and rainfall remotely from an active spaceborne instrument is explored.

1.2 Importance of Latent Heating

Latent heating is a thermodynamic process that releases or absorbs energy through a transitional change in the state of matter, first studied by Black (1770). In the atmosphere, it is prevalent in phase changes of water including condensation, freezing, deposition, evaporation, melting, and sublimation. Numerous studies have recognized the significance of latent heating within tropical regions. Aubert (1957) determined latent heat release affects vertical motion in the environment surrounding the release, with the maximum release height corresponding to the level of maximum velocity perturbation. Riehl and Malkus (1958) found that tropical convection provides the necessary means of transferring energy from the lower atmosphere to the upper troposphere, which feeds into the general circulation. This notion was based on the premise of "hot towers", a term coined in their paper for what today are considered to be turrets within the trimodal distribution of convection in tropical regions (Johnson et al., 1999).

Hartmann et al. (1984), with the use of linear models, later confirmed that the general circulation of the atmosphere is sensitive to the convection and associated latent heating occurring in tropical regions by widespread convection. To successfully recreate a circulation similar to that of the real atmosphere, the proper vertical velocity and heating profiles were required to be assumed in tropical regions. Similarly, Houze (1982) recognized the distinct importance of discerning cloud type when assigning a

top- or bottom-weighted nature of latent heating because of the differences in cloud characteristics between the regimes of tropical convection from shallow convection to stratiform coverage to overshooting towers. More recently, Handlos and Back (2014) calculated basis functions of vertical motion profiles using reanalyses and, coupled with observational datasets, derived the sum of latent heating and convergence of turbulent heat fluxes for different cloud types. Isolated systems of convection were shown to peak in the aforementioned sum closer to the surface than other regimes of convection and stratiform rain types, again signaling the marked difference in properties and dynamical effects between different modes of precipitation.

On a smaller-than-global scale, latent heating is a critical component to many atmospheric features, demonstrated by the sensitivity of models of various phenomena on the accurate diagnosis of latent heating. Schumacher et al. (2004) found that accounting for the spatial variability of cloud presence provided better simulations of climatic modes, like the El Niño Southern Oscillation, that affect the distribution of clouds compared to using simply a spatially invariable cloud cover representation. Furthermore, stratiform rain coverage in particular was a vital component to correctly modeling the general circulation. In the Madden-Julian Oscillation (MJO), latent heating by condensation within the lower levels of the atmosphere from shallow convection during the incipient stages causes a destabilization of the environment, allowing for the characteristic deep convection of later MJO stages to form (Jiang et al., 2011). A proper physical representation of this latent heating is therefore important

to correctly modeling the progression of atmospheric features like the MJO.

Moving poleward, the extratropics are directly affected by latent heating, augmenting the overall effects on the general circulation caused by latent heating in tropical regions. Martin and Otkin (2004) showed that the rapid formation of extratropical cyclones may be dependent specifically on the latent heat release that occurs with heavy precipitation. Latent heat release can also be a critical influence on whether weak extratropical cyclones grow and intensify or not (Zimmerman et al., 1989). Furthermore, extratropical forecasts are not immune to the effects of incorrectly estimating latent heating, as it has been shown that latent heating overestimation can result in overintensification of cyclone forecasts (Anthes and Keyser, 1979). Finally, moving to mesoscale magnitudes, some features of interest are largely the result of latent heating or cooling. An example is microbursts, a phenomenon of strong surface winds caused by downdrafts evaporating below the cloud base and accelerating towards the surface.

Latent heat has therefore been a motivating factor for research and remote observing platforms of the atmosphere. Simpson et al. (1988) posited that the three-dimensional structure of latent heating is crucial to modeling the general circulation for climate purposes, and that the Tropical Rainfall Measurement Mission (TRMM) satellite would provide detailed observations of latent heating. Because of its lower sensitivity

and larger field of view, however, TRMM does not often observe shallow precipitation and, in general, underestimates lighter precipitation compared to later ventures, namely CloudSat (Berg et al., 2010).

Unfortunately, a complete picture of latent heating is not straightforward as this apparent heating cannot simply be measured remotely. Diabatic processes occur throughout the atmosphere due to both radiative and thermodynamic effects, while amidst other land-atmosphere and atmospheric interactions. Therefore, proxies must be used to estimate the latent heat occurring in the atmosphere. Previous estimation methods will be discussed in Section 1.4.

1.3 CloudSat

CloudSat is an earth observation satellite flying in the Afternoon Constellation (A-Train). A-Train satellites fly at an altitude of 690 kilometers (km) and follow a sun-synchronous orbit that crosses the equator at around 1:30 P.M. local time. Figure 1.1 shows the satellites that make up the A-Train with the respective instruments aboard. The satellite of interest for this study, CloudSat, is equipped with a W-band (94 gigahertz (GHz)) microwave nadir-viewing radar named the Cloud Profiling Radar (CPR) (Stephens et al., 2008). The CPR has a vertical resolution of 480 meters (m) (with backscatter oversampling reducing this to 240 m), a cross-track resolution of 1.4 km, and an along-track resolution of about 1.5 km (Tanelli et al., 2008). The minimum detectible reflectivity of the CPR is -30 dBZ, providing the

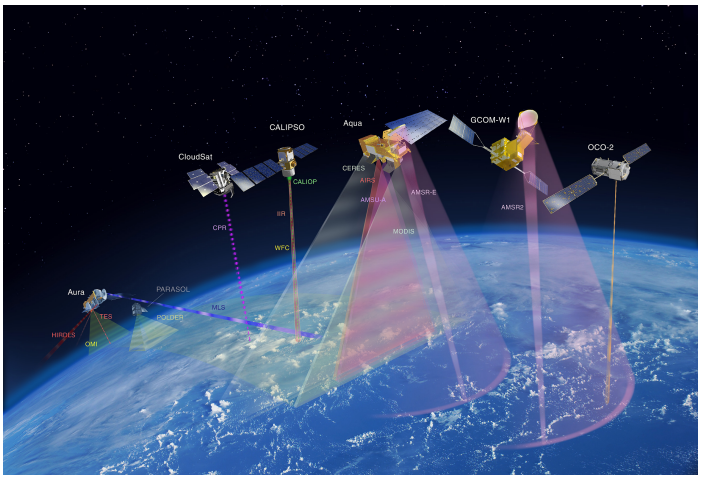

FIGURE 1.1: An illustration of the Afternoon Constellation (A-Train) satellite mission of NASA with the satellites' respective instruments. CloudSat is second from the left. Illustration courtesy of NASA.

sensitivity needed to observe thin and lightly precipitating clouds. A blind curtain exists below about 550 m, where bins from that level to the surface are contaminated with surface returns and thus unusable. Figure 1.2 shows an example of reflectivities from a segment of CloudSat orbit.

CloudSat's CPR provides a unique perspective for observing latent heat and precipitation because of its high sensitivity, in addition to both the resolution of the radar instrument and the satellite's colocation with other satellites in the A-Train. Currently, the CPR is used in an algorithm to generate estimates of precipitation over most of the globe through forward models (Haynes et al., 2009). These efforts have generated better estimates of stratiform rainfall in the tropics and overall precipitation in the extratropics, but the algorithm often underestimates heavier precipitation in the tropics due to full attenuation of the radar. Therefore, the synergy of using

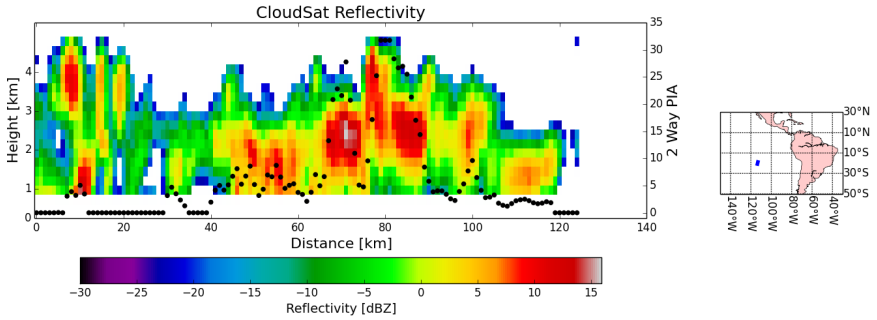

FIGURE 1.2: Sample reflectivity swath and two-way path integrated attenuation from CloudSat's CPR. This swath is taken from Granule 18422 on October 14, 2009.

the CPR with the TRMM Precipitation Radar (PR) to sense both the low and high ends of the precipitation spectrum provides a fuller picture of precipitation within the tropical regions (Berg et al., 2010). This hints at the potential for combined future latent heating and precipitation algorithms in the future (see Chapter 6 for more information).

1.4 Prior Latent Heating Estimates

In the past, regional studies such as Reed and Recker (1971) have attempted to model latent heating based on vertical motion, storage, and advection. Yanai et al. (1973) developed a methodology for deriving heat sources and sinks from an observing network (e.g. radiosondes) using budget equations similar to Reed and Recker. With these approaches, the ability to quantify latent heating occurring over an area from multiple observations became possible. Numerous studies have used this methodology since; in example, Schumacher et al. (2008) estimated the latent heating that occurred

in the Marshall Islands region through radiosonde observations. Field campaigns like the VAMOS Ocean Climate Atmosphere and Land Study-Regional Experiment (VAMOS-REX) and the North American Monsoon Experiment provide observations that can be used to estimate latent heating with a radar-based measurement (Mechoso et al. (2014); Higgins and Gochis (2007)).

However, the greatest source of large-scale latent heat estimates has been the TRMM satellite. Multiple latent heating algorithms have been assembled for use with the TRMM PR. A brief description is provided of each, while an exhaustive review of the algorithms can be found in Tao et al. (2006).

The Goddard Convective-Stratiform Heating product (Tao et al., 1993) uses rain rate as a proxy for cloud depth and includes cloud type to retrieve a latent heating profile out of a lookup table constructed from CRM simulations. The Hydrometeor Heating product (Yang and Smith, 1999) uses the profile of cloud drops along with vertical velocity and rain rate to perform an inverse calculation from a cloud-resolving model (CRM). The Precipitation Radar Heating product (Satoh and Noda, 2001) uses the profile of reflectivity along with vertical velocity and rain rate to calculate the latent heating based on thermodynamic relationships. The TRAIN algorithm (Olson et al., 1999) trains a database of reflectivity and brightness temperature, used to estimate a latent heating profile based on an observed brightness temperature from the TRMM Microwave Imager. The Spectral Latent Heating (SLH) product (Shige et al., 2004)

uses characteristics of the reflectivity profile to retrieve a latent heating profile out of a lookup table constructed from CRM simulations.

The final product, SLH, is the template for this algorithm because it lends itself very well to application to other satellite, ground, or airborne radar platforms from which the parameters can be obtained. SLH uses parameters like the classification of precipitation regime, precipitation top height, and precipitation rates at the melting layer and surface to choose a latent heating profile from a lookup table based on CRM simulations. Where this study's new algorithm differs from SLH is in the selection methodology, instead using a Bayesian approach that provides a mean state with an uncertainty based on the distribution of the retrieval.

1.5 Bayesian Methodology

Bayesian retrievals have been used successfully in the past because of the flexibility in using prior physical information to constrain the retrieval and the synergy of combining different measurement types where applicable. Early examples of satellite algorithms using Bayesian methodologies with model-generated states include Mugnai et al. (1993), implementing a version of the Colorado State University and University of Wisconsin Regional Atmospheric Modeling Systems on passive microwave radiances; Evans et al. (1995), using the Colorado State University Regional Atmospheric Modeling System on passive microwave radiances; and Olson et al. (1996), employing the Goddard cumulus ensemble model for a combined active-passive retrieval.

1.6 Study Objective

There remains a gap in the estimation of latent heating globally because of a lack of observation of light precipitation and shallow clouds from conventional precipitation sensors. The main objective of this study is to test the hypothesis that latent heating in lightly precipitating warm rain clouds can be constrained algorithmically by exploiting the CloudSat CPR. The algorithm will create snapshots of latent heating in time that, when composited and gridded, can generate latent heating estimates over the ocean from shallow convection.

Construction of the algorithm is discussed in Chapter 2. Results from the algorithm in a synthetic environment are shown in Chapter 3. Chapter 4 contains applications of the algorithm to observational datasets from field campaigns and CloudSat. The ability to answer the study objective is ultimately assessed in Chapter 5. Forthcoming research and potential avenues of algorithm advancement are highlighted in Chapter 6.

Chapter 2

Algorithm Design

2.1 Introduction

To fulfill the study objective, a retrieval for latent heating in shallow, warm rain clouds using characteristics of the reflectivity profile is constructed. A cloud-resolving model combined with a radar simulator is implemented to construct a database of profiles that are composed of all associated variables including latent heating, reflectivity, and attenuation. The algorithm uses a Bayesian framework that takes in a reflectivity profile with ancillary information and generates a latent heating profile, liquid water path, and surface rain rate from the database with associated uncertainties. Figure 2.1 is a schematic representation of the whole algorithm system.

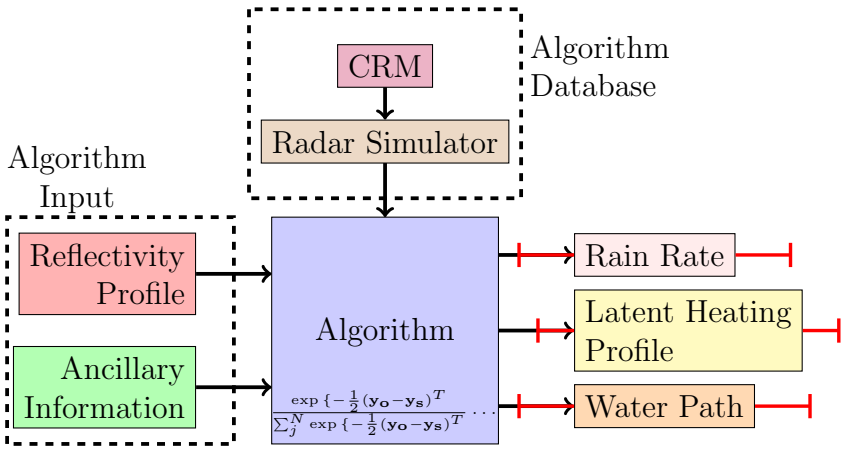

FIGURE 2.1: Schematic of the algorithm system. The algorithm database is built prior to use and remains static. Algorithm input on the left is composed of the reflectivity profile and ancillary information. The output shown on the right includes rain rate, latent heating, and liquid water path with uncertainties.

2.2 Cloud-Resolving Model Simulations

2.2.1 Model Configuration

Central to the Bayesian retrieval approach is a database spanning the space of realistic cloud states that have rain profiles and associated observables. To generate this database, the Regional Atmospheric Modeling System (RAMS) is employed. RAMS is a versatile high resolution, non-hydrostatic, two-moment bulk microphysics cloud-resolving model that includes cloud and precipitation microphysics at a fine resolution (Cotton et al., 2003). Moments defining the microphysics are the mixing ratio and number concentration of each hydrometeor type.

Seven hydrometeor species are defined in RAMS: cloud droplets, drizzle, rain, pristine

ice, graupel, hail, and aggregates. For this study, only liquid species are used as the focus is on warm rain processes. Species are defined by size distributions that follow a modified gamma distribution, while mass-volume and terminal velocity relationships follow a power law. RAMS utilizes heat budget equations that conserve energy and track the heat storage and release associated with mass exchanges between all hydrometeor species, allowing the contributions of specific microphysical processes to the total latent heating to be separated. Model domain, resolution, and boundaries are scalable to apply the model to any environment or phenomenon.

Simulations are initialized from composite soundings of the Atlantic Trade Wind Experiment (ATEX) over a domain in the tropical Atlantic Ocean, ranging from 14.49^o N to 15.39^o N and from 35.53^o W to 36.46^o W (Augstein et al., 1973, 1974, Saleeby et al., 2014, Stevens et al., 2001). The model resolution for all simulations is set to 250 m horizontally and 100 m vertically. Each horizontal direction contains 400 points spanning a 100 km distance, while 40 vertical layers extend to 4 km above the surface.

Nine separate simulations are used to build the database. Sea surface temperature (SST) and cloud condensation nuclei concentration (CCNC) are both varied for each run, with SST between 293 Kelvin (K), 298 K, and 303 K and CCNC between 100 per cubic centimeter (cc), 400 cc, and 800 cc. Lower SSTs correspond with stabler environments, while higher SSTs represent more unstable environments. Lower CCNCs signify cleaner environments and dirtier environments are represented by higher

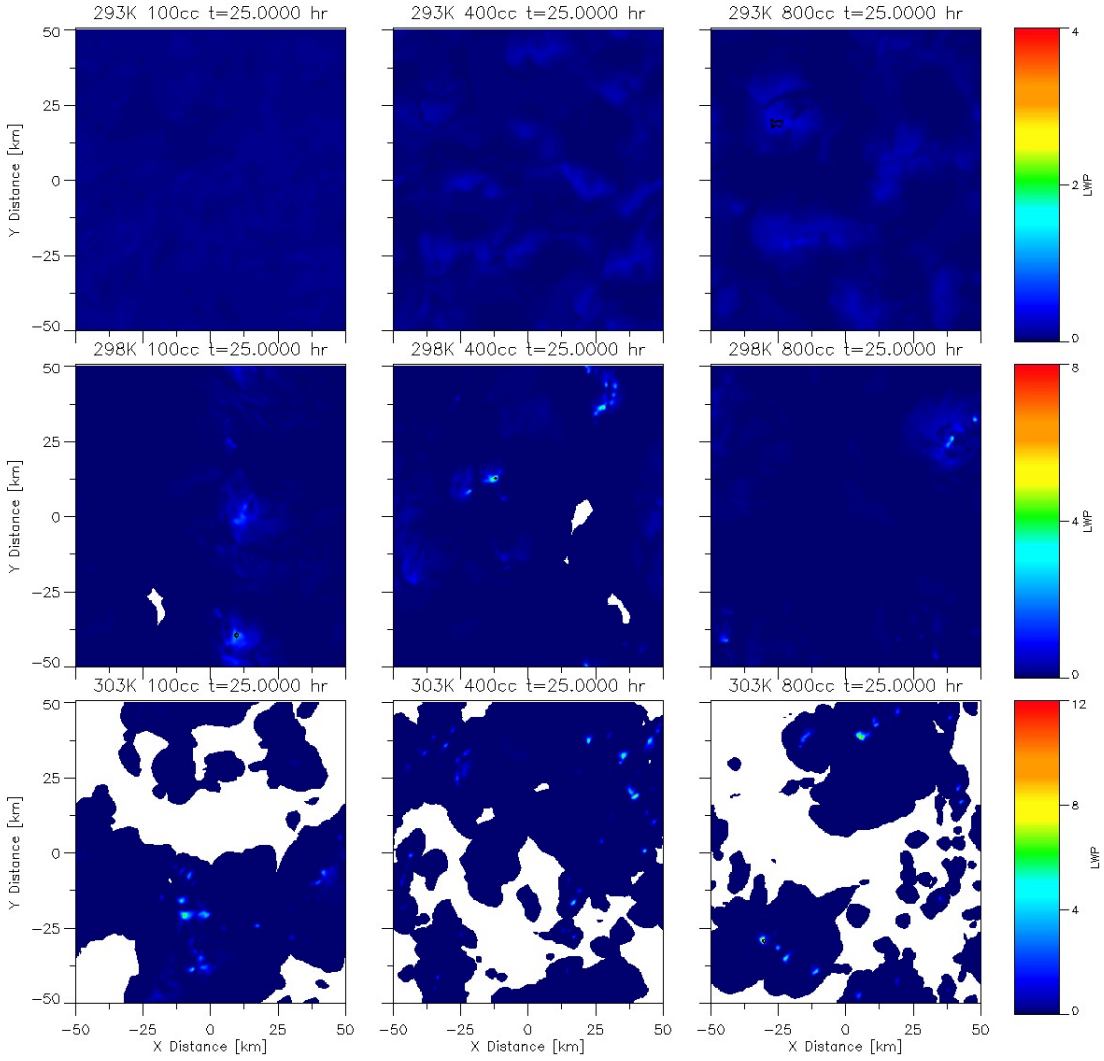

FIGURE 2.2: Liquid water path of each simulation is contoured in color.

CCNCs. This range of atmospheric characteristics create a variety of atmospheric states, designed to capture variability that exists within the real atmosphere (van den Heever et al., 2006).

2.2.2 Simulation Characteristics

Figure 2.2 shows the typical patterns of precipitation between different simulations for one time step under a number of distinct environmental conditions. For lower SSTs, the rain is very homogenous in extent, with a few areas of slightly convective areas favoring the dirtier environments. The environments with higher CCNC have more areas of enhanced precipitation, while lower CCNC environments have fewer precipitation cores and instead contain more homogeneously raining cloud cover. At higher SSTs, much of the domain is rain free as precipitation is confined to limited stratiform areas surrounding a few isolated cores. Higher CCNC environments have an even lower spatial extent of rain due to the suppression of precipitation by increased aerosols. Areas where it is raining at higher CCNCs are more intense than lower CCNCs, and is somewhat analogous to the aerosol indirect effects of increasing CCNC described by Twomey (1974, 1977). Herbener et al. (2014) point out the difference in response to CCNC between SSTs is the result of the stable cloud layer in the 293 K simulation. It is only at greater CCNCs that the agglomerated cumulus clouds are able to penetrate above the layer.

In fact, a comparison of rainfall efficiency, defined as the probability of precipitation for a given liquid water path, demonstrates that increasing aerosol concentration induces a similar shift toward lower rain fraction when SST is increased. Figure 2.3 displays this graphically. The lowest SST case activates precipitation at lower

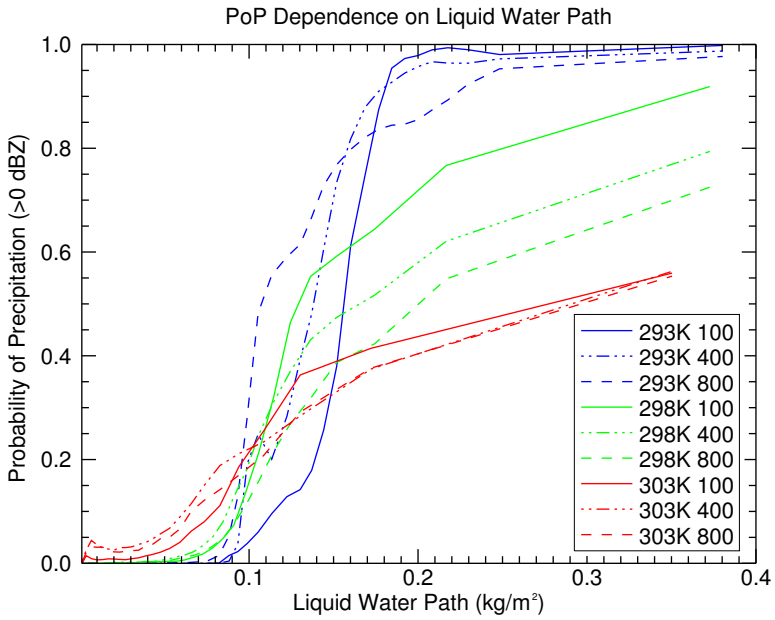

FIGURE 2.3: Functions of liquid water path versus precipitation efficiency (defined as a profile reaching 0 dBZ) for simulations included in the database.

liquid water paths for higher CCNCs, but at the more unstable SSTs the aerosol acts to suppress precipitation towards higher liquid water paths. Furthermore, at the intermediate SST, CCNC is the determination whether more homogenous (higher efficiencies) or convective (lower efficiencies) precipitation is present. This is consistent with Saleeby et al. (2014) who note that the wide ranging spectrum of regimes at the intermediate SST is the result of CCNC causing increases in water droplet number concentrations. Simulations dominated by thin clouds therefore see a decrease in precipitation for higher CCNC by cutting off the thinly precipitating clouds, while simulations characteristic of taller convection will have enhanced precipitation with increased CCNC. Where the intermediate SST differs from the lowest SST case is

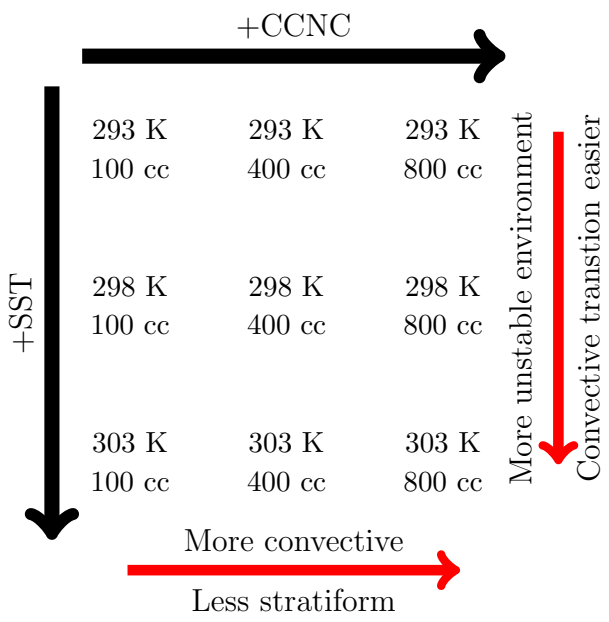

FIGURE 2.4: Qualitative model of the relationships between SST and CCNC for the nine model simulations included in the database.

that the environment is at a conditional instability that allows convective regimes to not only penetrate the homogeneous deck, but deepen further to the point of raining intensely. Figure 2.4 qualitatively displays the discussed variations between the nine simulations.

2.3 Radar Simulator

Output from the RAMS model provides diagnostic and prognostic variables for hydrometeors and the atmospheric state. To transfer this output to a set of observables that might be seen by a radar surveying the real atmosphere, the model scene can be "observed" through a radar simulator that uses these model variables. The QuickBeam radar simulator is a well-documented and tested forward model that computes

reflectivities and attenuation for a given radar frequency from hydrometeor profiles (Haynes et al., 2010). Microphysical distributions assumed in QuickBeam match those of the RAMS simulations. For the extent of this study, Quickbeam is used to simulate CloudSat (94 GHz; W band) and no Doppler information is used. The resulting profiles of attenuated reflectivity are used directly to eliminate dependence of the algorithm on derived attenuation corrected CloudSat data products. Because the algorithm is restricted to only warm (liquid phase) clouds, droplets are assumed to be spherical and of constant density when calculating reflectivities.

2.4 Database Properties

To create the algorithm database, every eighth timestep is sampled to provide an eligible pool of profiles. For a profile to be included in the database, the maximum reflectivity of the profile must be at least 0 dBZ (a threshold used by CloudSat to indicate rain is certain). Two different databases are created by modifying the resolution of the profiles. The first database is assembled at model resolution, whereby the profile is treated as a sole profile with 250 m horizontal and 100 m vertical resolution.

Because the aim of this study is an application to CloudSat, a second database is created and upscaled to the resolution of CloudSat: each point is averaged with surrounding points to construct a circular footprint of 1.5 km by 1.5 km and vertical levels are averaged to form 300 m vertical bins. Both databases are used in testing, but the second will ultimately be adopted for the application to CloudSat observations

as it provides an appropriate comparison of scales. Even after sub-sampling the model in this way, the model resolution database has approximately 1.4 million profiles and the CloudSat database has 1.25 million profiles, a smaller number as a result of edge averaging effects. Profiles on rain core edges are averaged with surrounding profiles that do not reach 0 dBZ, bringing the Cloudsat resolution profile under the dictated 0 dBZ minimum reflectivity. This edge smearing effect decreases the sharpness of storm extents as occurs when real world precipitation is averaged over the CloudSat field of view.

Figure 2.5 shows the average latent heating structure of the database simulations binned in 100 m intervals and sorted by the 0 dBZ height from the top of the profile. As expected, lower SST environments are characterized by very shallow latent heating profiles, not exceeding about 1.5 km above the surface. At higher SSTs, profiles tend to get deeper with increasing 0 dBZ heights since this parameter is representative of the vertical extent of precipitation-sized drops. The broad layer of heating is due to condensation at lower levels, evaporative cooling near the cloud top is due to entrainment of drier air, and cooling near the surface is from evaporative cooling of rainfall.

2.5 Parameters Tested

Key characteristics of the profile are chosen as parameters representative of the physical processes occurring in the profile. Figure 2.6 shows an example cross section

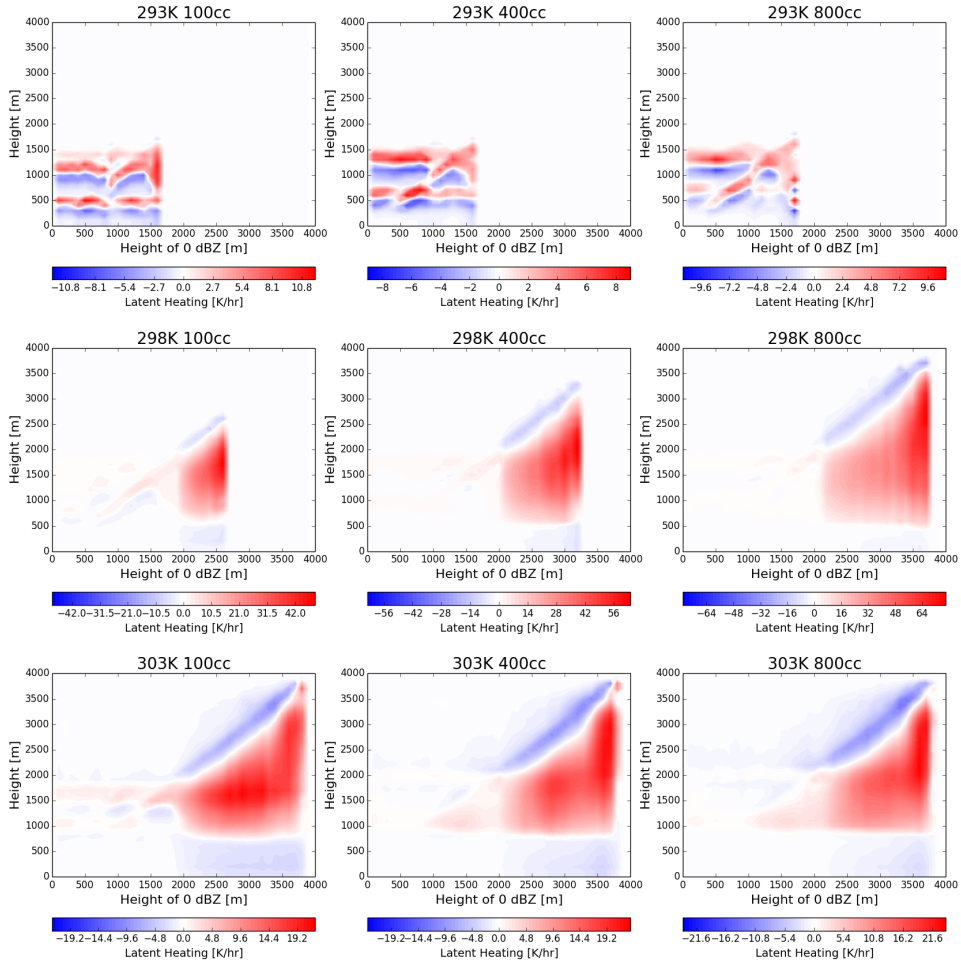

FIGURE 2.5: Contoured average vertical latent heating structure for each simulation in the database sorted by the height of 0 dBZ from the top. Note the different color bar ranges for each plot.

of input reflectivity and the calculated parameters. From the top of the cloud, the height of intersection with -30 dBZ represents the cloud top level. Next, the height of intersection with 0 dBZ is chosen to indicate the top of the area certainly with rain. Additionally, the height of the 0 dBZ intersection starting from the bottom of the profile going up is used to provide a measure of the vertical distribution of rain and attenuation within the cloud. For example, clouds with weaker attenuation may have

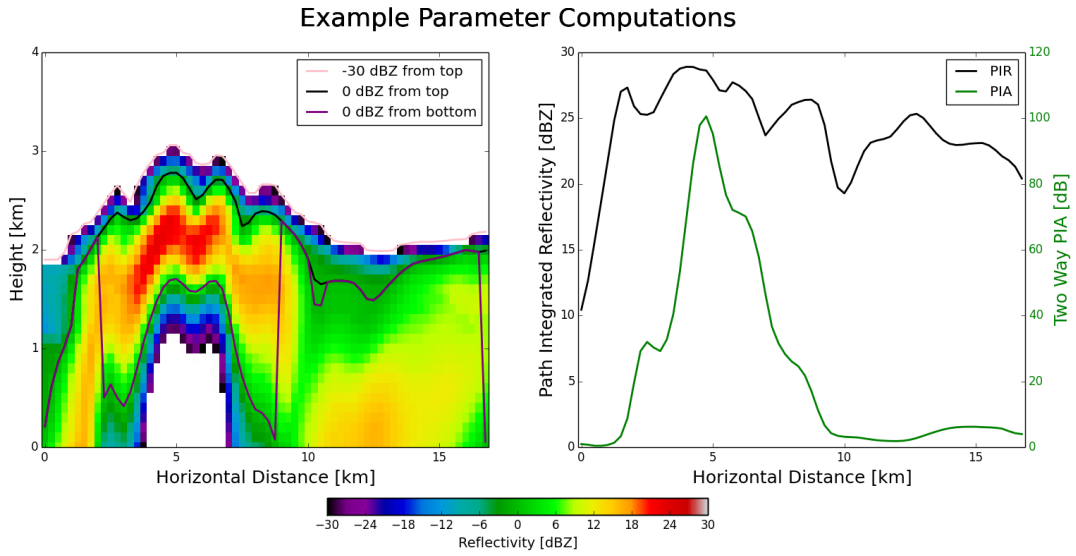

FIGURE 2.6: Example cross section of input reflectivity and the associated parameters used in algorithm computations.

Parameter	Physical meaning	Error Assumed
-30 dBZ height from the top	Cloud top height	100 (300) m
0 dBZ height from the top	Rain top height	100 (300) m
0 dBZ height from the bottom	Vertical rain structure	100 (300) m
Near-surface reflectivity	Near-surface activity	1 dBZ
Path integrated reflectivity	Total drop spectrum	1 dBZ
Path integrated attenuation	Intensity of drops	1 dB

TABLE 2.1: List of parameters used in the algorithm, microphysical property represented by each, and the error assumed at model (CloudSat) resolution.

0 dBZ intersections from the top and bottom that match, as the profile remains above 0 dBZ through the depth of the cloud. Alternatively, the profile could drop below 0 dBZ near the surface (indicating drizzle), causing the 0 dBZ intersection from the bottom to be very low. Profiles with stronger attenuation will have the 0 dBZ level from the bottom occur near the levels of strongest attenuation.

Next, the path integrated reflectivity (PIR) serves as a measure of the total cloud drop

spectrum within the cloud. Two way path integrated attenuation (PIA) provides information about the density of water drops within the cloud; denser clouds will attenuate more as they degrade the power of the radar pulse traveling through the cloud. Finally, the lowest clear bin of reflectivity provides an additional measure to constrain near-surface interactions for profiles that have not been fully attenuated. These parameters are summarized in Table 2.1.

2.6 Bayesian Theory

Bayesian retrieval methods are foundationally based on Bayes' theorem, which says the probability of a state given an observation is proportional to the product of the probability of the observation given the state and the occurrence of the state, i.e. $p(\mathbf{X}|\mathbf{Y}) = p(\mathbf{Y}|\mathbf{X}) * p(\mathbf{X})$. Generally speaking, a Bayesian retrieval takes an initial state (or an *a priori distribution*) and updates (or *constrains*) it to a new state (or *posterior distribution*) given a set of observations. A qualitative illustration of this is shown in Figure 2.7.

For this algorithm, $\mathbf{Y}$ is the vector of reflectivities from CloudSat and $\mathbf{X}$ is the vector of the atmospheric state including latent heating, rain rate, and liquid water path. To generate the retrieval, each database member's parameters $\mathbf{y_s}$ are compared to the input profile's parameters $\mathbf{y_o}$, and a probability is assigned to the member. The probability is a function of the difference between the member and the input, accounting for the covariance in the database $\mathbf{S}$ and the observations $\mathbf{O}$. This is a calculation

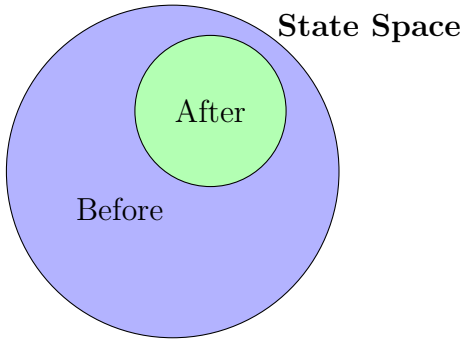

FIGURE 2.7: An illustration of the concept of Bayesian retrievals. An initial state space is constrained by a set of observations to a new state.

after Evans et al. (1995) and L'Ecuyer and Stephens (2002):

$$p_i = \frac{\exp\left\{-\frac{1}{2}(\mathbf{y_o} - \mathbf{y_s})^T(\mathbf{O} + \mathbf{S})^{-1}(\mathbf{y_o} - \mathbf{y_s})\right\}}{\sum_j^N \exp\left\{-\frac{1}{2}(\mathbf{y_o} - \mathbf{y_{s,j}})^T(\mathbf{O} + \mathbf{S})^{-1}(\mathbf{y_o} - \mathbf{y_{s,j}})\right\}}, \tag{2.1}$$

where N is the number of database members and T is the matrix transpose. Covariance errors are determined based on the assumption that all variables are independent. Errors are assigned to be consistent with the characteristics of the CloudSat CPR (Tanelli et al., 2008). Reflectivity and PIR are assumed to have an error of 1 dBZ to match the CloudSat PR; two way PIA is assumed a similar 1 dB error. Height errors are assumed to match one vertical level of the algorithm, 100 m for model resolution and 300m for CloudSat resolution.

The output of the algorithm is then a weighted sum of the database:

$$M = \sum_{i=1}^{N} y_{s,i} * p_i. \tag{2.2}$$

With each output, the Bayesian uncertainty is the weighted standard deviation of the database from the output (retrieved mean):

$$U = \sqrt{\sum_{i=1}^{N} (y_{s,i} - M)^2 * p_i}. \tag{2.3}$$

A Bayesian retrieval provides the infrastructure to combine measurements of different types and from different instruments. Further, the retrieval combines not only the mean state but also uncertainty in that mean through the prescribed error estimates. No assumptions regarding physical characteristics of the profile, such as an assumed cloud droplet number concentration of the profile, are required because thermodynamic and dynamic constraints are instead imposed through the model physics.

2.7 Information Content

Information content (IC) metrics can be used to assess the effect of adding or removing inputs into the algorithm system. Such metrics derive from the original work of Shannon and Weaver (1949), who introduced the idea of using changes in entropy as a quantitative measure of information. Following the methodology outlined in Rodgers (2000) and L'Ecuyer et al. (2006), the application of this termed Shannon Information Content (SIC) framework in comparing retrieval configurations is described.

SIC collapses the observing system characteristics into a scalar quantity that represents their resolutions within the parameter space, taking into account both the sensitivity of the instrument measurement and any uncertainty in the retrieval. Uncertainties can result from either measurement noise or model error in the database components. The typical application of information theory involves assuming that both states measured can be represented by Gaussian distributions, in which case H can be defined in terms of the error covariances of the prior and posterior states, $\mathbf{S_a}$ and $\mathbf{S_x}$, respectively:

$$H = \frac{1}{2} log_2 |\mathbf{S_a} \mathbf{S_x}^{-1}|. \tag{2.4}$$

The Bayesian algorithmic setup, however, allows this assumption to be relaxed. Entropy of a state can then be calculated using the database of probabilities by

$$S(P) = -\sum_{i}^{P} p_i log_2 p_i. \tag{2.5}$$

The SIC, denoted H, is defined as the difference in entropies between two states, P_1 and P_2:

$$H = S(P_1) - S(P_2), \tag{2.6}$$

providing a quantitative assessment of the information change between two states. Lower values of SIC represent an *increase* in information by the second state compared to the first. For this study, $S(P_1)$ is defined as the retrieval using no inputs; each database member is assigned a probability of $\frac{1}{N}$ with N the number of members.

Chapter 3

Initial Retrieval Results

3.1 Introduction

The performance of the algorithm will be assessed through a combination of synthetic retrievals and application to radar observations. Synthetic retrievals will be conducted over cross sections and full domain time steps not used in the construction of the database in this chapter. Comparisons will be made between the model resolution and CloudSat scales to provide insight into the effects of resolution degradation and to determine whether the algorithm performs similarly with a CloudSat-sized footprint. To examine the behavior of the algorithm in real-world scenarios, the algorithm is applied to W-band radar observations collected during the VOCALS-Regional Experiment and a selected CloudSat orbit in Chapter 4.

3.2 Conditioning of the Database

As mentioned in Chapter 2, the algorithm is built on the use of six parameters representing physical components of each profile. It might be expected for the algorithm to simply take an input of the full reflectivity profile instead of collapsing the profile into a few parameters, as this would provide the most information about the complete profile extent. The best way to resolve this is to compare the performance of the algorithm in both cases. So, the cross section initially depicted in Figure 2.6 is input into the algorithm using the full reflectivity profile and the resulting output is shown in Figure 3.1. This cross section is taken from the 298 K 400 cc simulation. Again, no profiles from this cross section were directly included when generating the retrieval database.

The top row of Figure 3.1 displays the model latent heating profiles, average model latent heating profile, and the QuickBeam reflectivity profiles and two-way PIA associated with the cross section. The middle row of figures shows the retrieved latent heating profiles, average retrieved latent heating profile, and liquid water path both from the model–the so called "truth"–and the retrieval. Yellow shading indicates the algorithm uncertainty in the retrieval (the weighted standard deviation output in Equation 2.3). Horizontal lines indicate the mean value of the quantity across the cross section, with color and line type corresponding to the legend in each plot. The bottom row displays the model and retrieved column-averaged latent heating, SIC

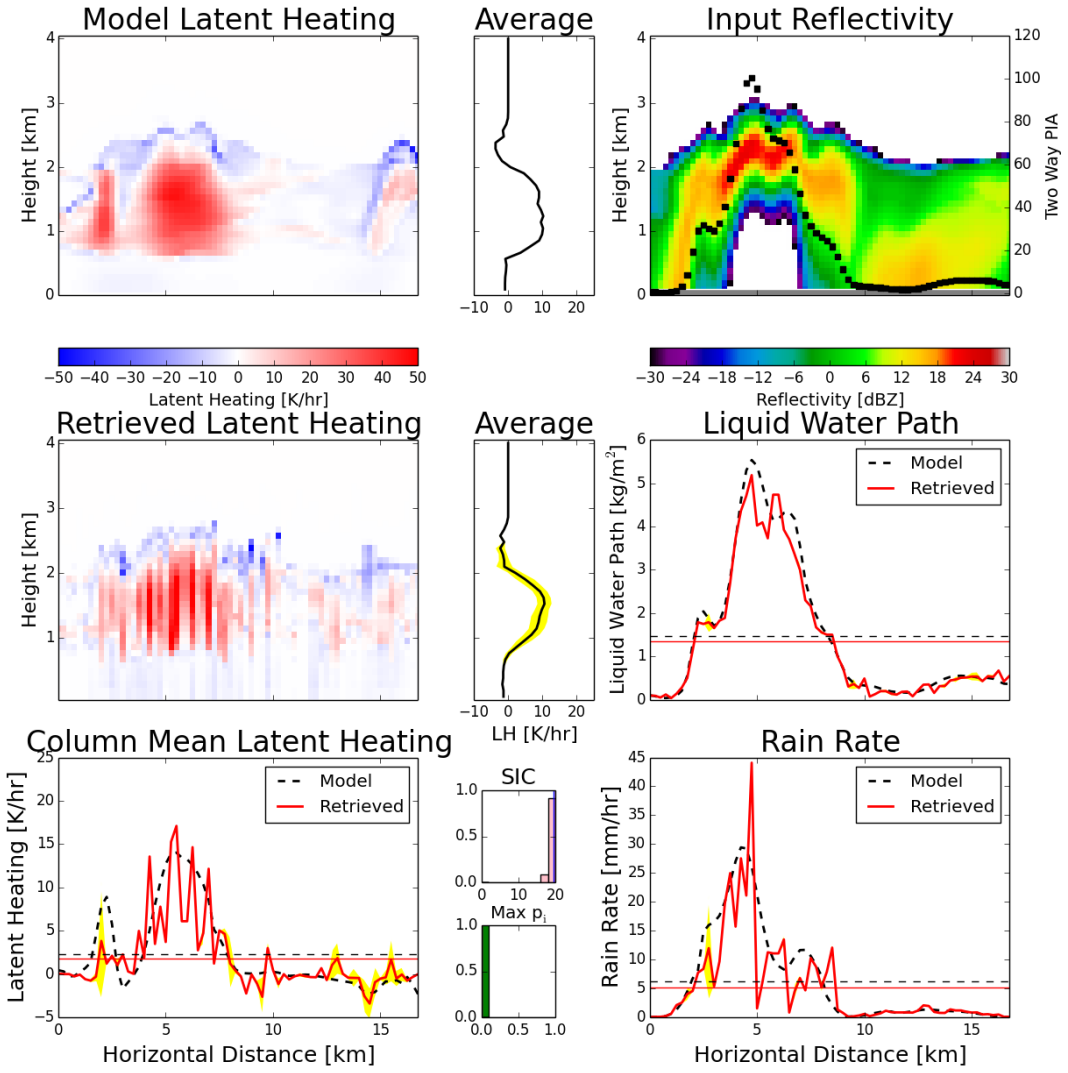

FIGURE 3.1: Demonstration retrieval using the full reflectivity profile. The top row shows the model vertical distribution of latent heating in the scene along with the reflectivity input into the algorithm. The middle row shows the algorithm retrieval of the vertical distribution of latent heating, the average vertical profile of latent heating, and liquid water path from the model and retrieval. The bottom row shows the model and retrieval column average latent heating, information content and profile total unnormalized probability distributions, and the model and retrieval rain rate. Yellow shading indicates one standard deviation of the retrieval uncertainty.

distribution of profiles in the cross section (see Section 2.7), distribution of maximum probability of profiles prior to normalizing (in this case, analogous to the chi-squared value: $max(p_i) = \exp\{-1/2 * max(\chi^2)\}$, with generally $\chi^2 = (y_o - y_s)^2/(O + S)$), and the model and retrieved surface rainfall rate.

Three cells are present, with the largest centered around the 5 km horizontal mark. The average latent heating profile reveals cooling at the top of the cells at 2.2 km and an area of heating through the middle extent of the cloud from just below 1 km to 2 km. Very slight cooling is also occurring below the cloud base down to the surface. This profile represents an overall heating in the cloud due to precipitation formation, cooling near the top due to entrainment, and cooling below the cloud base from evaporation of precipitation. Retrieved quantities are very noisy across the domain in regards to both the vertical profiles of latent heating and the column-averaged latent heating. Liquid water path is smoother and, though generally following the trend of the model quantity, adds an incorrect peak to correspond with an erroneous peak in rain rate. In fact, the rain rate spikes to almost 150 % of the model value near the 5 km horizontal mark. SIC values remain near the maximum value of 20 indicating no information is contained in the retrieval.

The simulations that make up the database provide discrete possible states of the atmosphere, not a type of continuous function that is fitted to observations or theory providing a relationship between two values. Choosing a retrieval process that

ingests all levels of the reflectivity profile requires a database that spans the complete distribution space for each dimension of the observation. Uncertainties for each of the retrieved values in this case were very low or non-existent because the database does not completely span this space. As a result, the lack of uncertainties is not due to strong confidence by the algorithm in the retrieval but instead due to a lack of possible matches.

It is more obvious to look at this from a chi-squared perspective. Very low non-normalized probabilities correspond to high values of chi-squared and describe a bad fit. By constraining a database of quantum profiles of reflectivity with an equal number of parameters as observations, areas of the distribution that do not span all values of a given dimension will cause non-normal behavior. The algorithm will retrieve a profile between two distinctly different states, causing the retrieved answer to jump to one extreme as it is on a tail end of the distribution. Without an associated uncertainty, the retrieval simply turns into a nearest neighbor search in the database. This stresses the importance of using a set of parameters within the Bayesian framework whose dimensionality is captured in the database, which relaxes the discontinuous nature of the database.

3.3 Synthetic Retrievals

3.3.1 Model Resolution Retrievals

With the use of parameters established, and to distinguish the behavior of the Bayesian inversion scheme from spatial averaging effects, algorithm performance is now explored in a synthetic retrieval environment at the native resolution of the RAMS simulations.

3.3.1.1 Example Cross Section

Figure 3.2 displays the results of the application of the algorithm with the six parameters defined in Section 2.5. Heating within the largest cell is represented with cooling at the top of the cloud. The secondary cell to the left is also captured by the algorithm, with a slightly shallower layer of heating and associated cooling above the cloud. Cooling is also placed below the cloud base, with stronger cooling corresponding to the more intense part of the largest cell. Finally, the dissipating cell on the right edge of the cross section is represented by shallow heating centered around 1.5 km and cooling near the top of the cloud. The average latent heating profile captures heating through the middle extent of the cloud, including a peak near 1.7 km. Cooling at 2.2 km corresponds to cooling at the same level in the model, with the algorithm uncertainty capturing the truth profile. The algorithmic average profile has a more

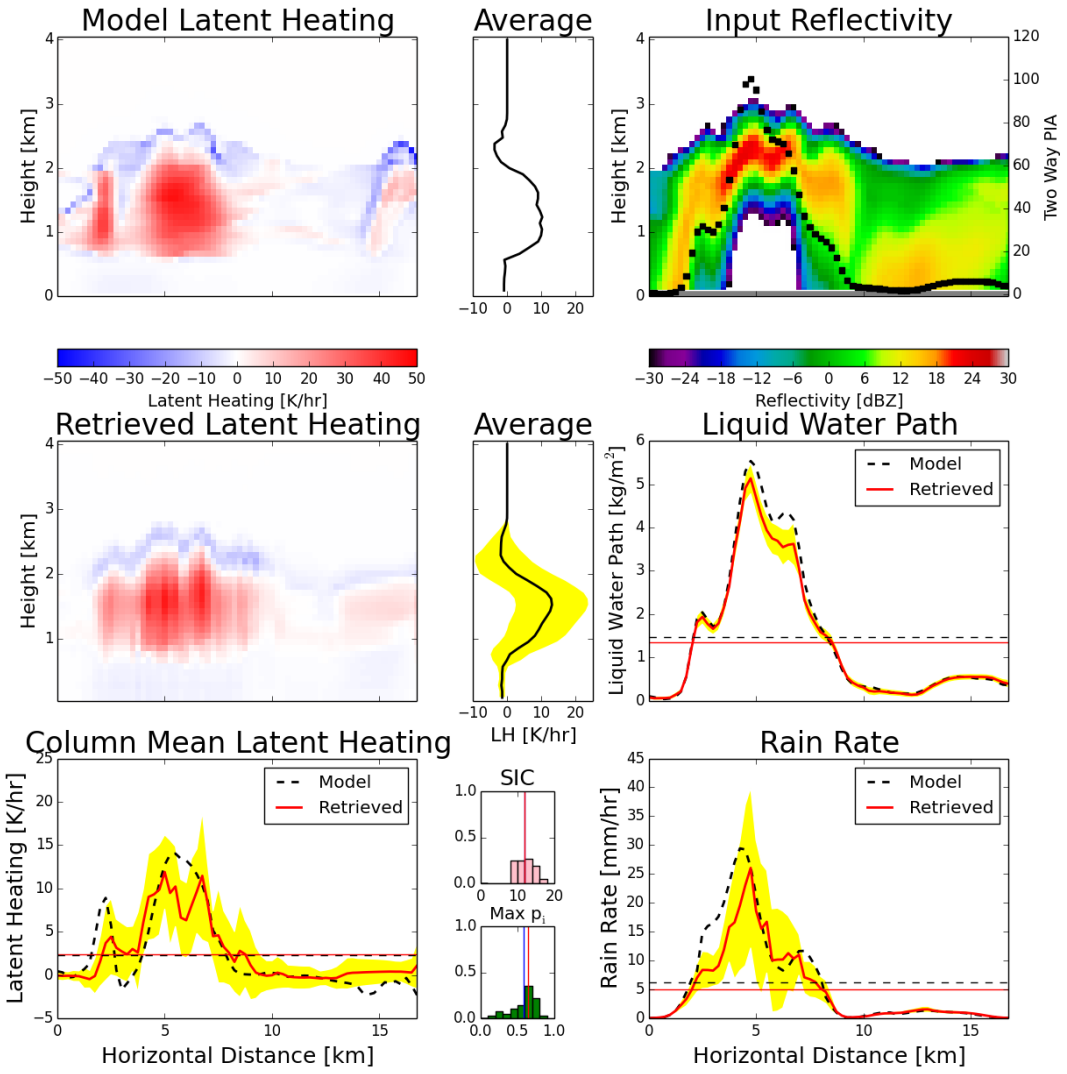

FIGURE 3.2: Same as Figure 3.1 but using the algorithm parameters instead of a full reflectivity profile.

peaked heating profile compared to the model, but the uncertainty again captures the modeled values.

There is nearly complete agreement between the model and the algorithmically retrieved liquid water path, with the model mean LWP slightly underestimated by the retrieval. Column mean latent heating has the large-scale features of the cross section represented well. The strong heating from the largest cell is retrieved, as is the lack of heating between the two clusters of cells from 10 km to 13 km. Overall cooling is not retrieved as strongly in the far right cell or between the two left cells, but that is compensated for by some underestimation of heating in areas, showing very little bias in the retrieval mean column-averaged latent heating. Additionally, the general features of the rain rate are captured by the algorithm. The strongest regions of rain rate are picked out, as are the areas of very light rain near the dissipating cell.

3.3.1.2 Full Domain Results

The algorithm is run on a full model time step (not included in the database) from the 298 K 800 cc simulation and the results are shown in Figure 3.3. On a first order, the algorithm retrieves the spatial structure of storms, placing the strongest rain rates along the 50 km line from the western edge, with heating in the same areas. The furthest north cell near 35 km from the southern edge is also a cell of heating and the lack of a high rain rate is placed correctly, confirming the algorithm does not simply

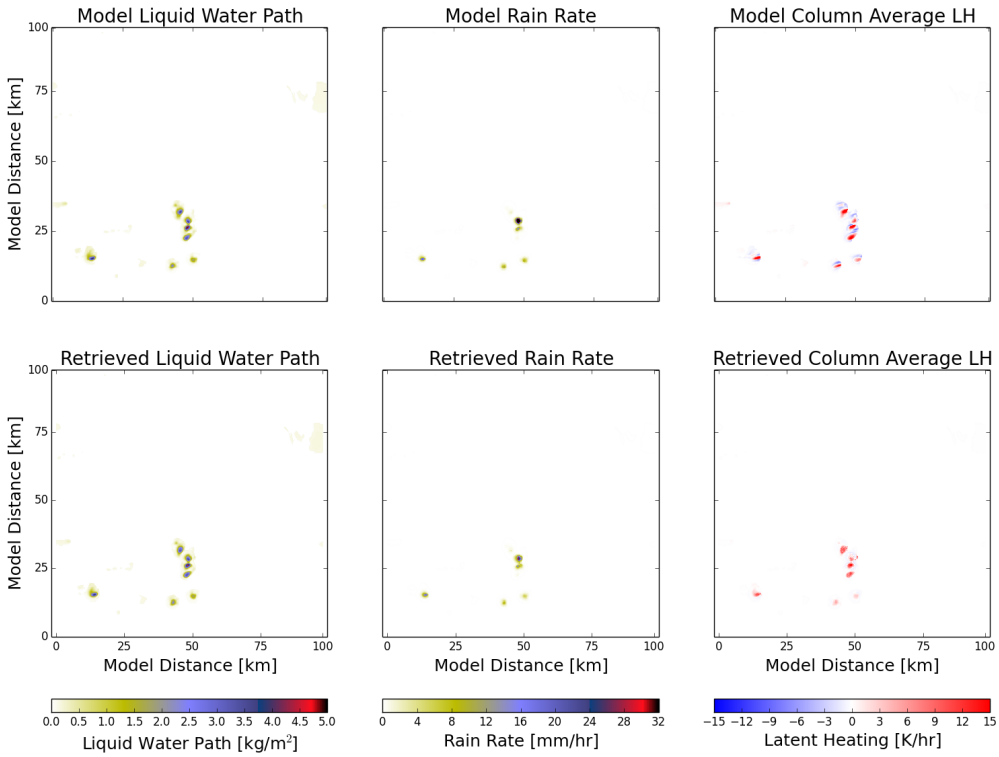

FIGURE 3.3: Model resolution retrieval of liquid water path, rain rate, and column mean latent heating for a 298 K 800 cc time step.

retrieve a high rain rate in areas of the most intense heating. Areas of column mean cooling are not as well retrieved around the edges of cells, but that is made up for some by an underestimation in heating. Figure 3.4 is a set of scatter plots between model and retrieved values of liquid water path, rain rate, and column-averaged latent heating.

LWP is retrieved fairly well, with the scatter plot following a 1:1 ratio between modeled and retrieved. The domain LWP root mean square error (RMSE) is 0.079 kg/m^2 and the bias is 0.008 kg/m^2 (1.86 %). Rain rates have a RMSE of 1.902 mm/hr and are

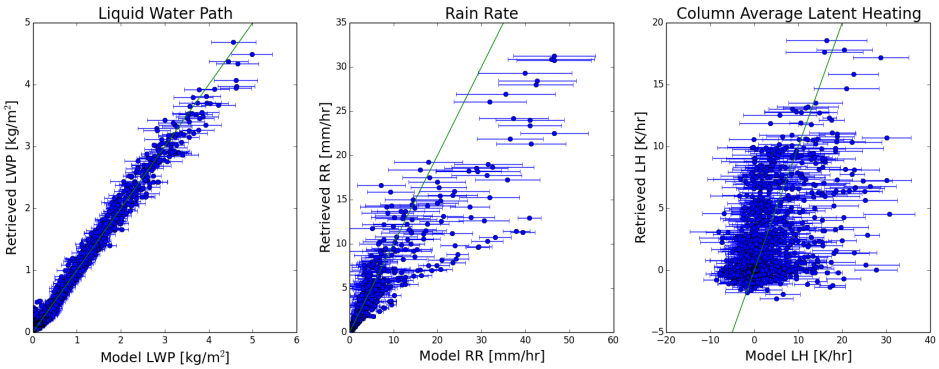

FIGURE 3.4: Model resolution retrieval error of latent heating, liquid water path, and rain rate for a model time step. Lines with a slope of unity are plotted in green for reference.

biased 0.227 mm/hr below the average (-0.227 mm/hr, -21.35 %). At lower rain rates, the retrieval straddles a 1:1 ratio, while higher rain rates are biased lower, likely due to the attenuation effects of W band radar. Latent heating has a RMSE of 2.975 K/hr and bias of 0.080 K/hr (13.09 %); errors of over- or under-estimation are mostly balanced out across the 100 km by 100 km domain, with a slightly higher mean latent heating being retrieved.

3.3.2 CloudSat Resolution Retrievals

Now that the effect of the use of parameters instead of the full reflectivity profile has been isolated, the algorithm performance is measured with the degradation of the retrieval resolution to one appropriate for the CloudSat CPR in the synthetic retrieval environment.

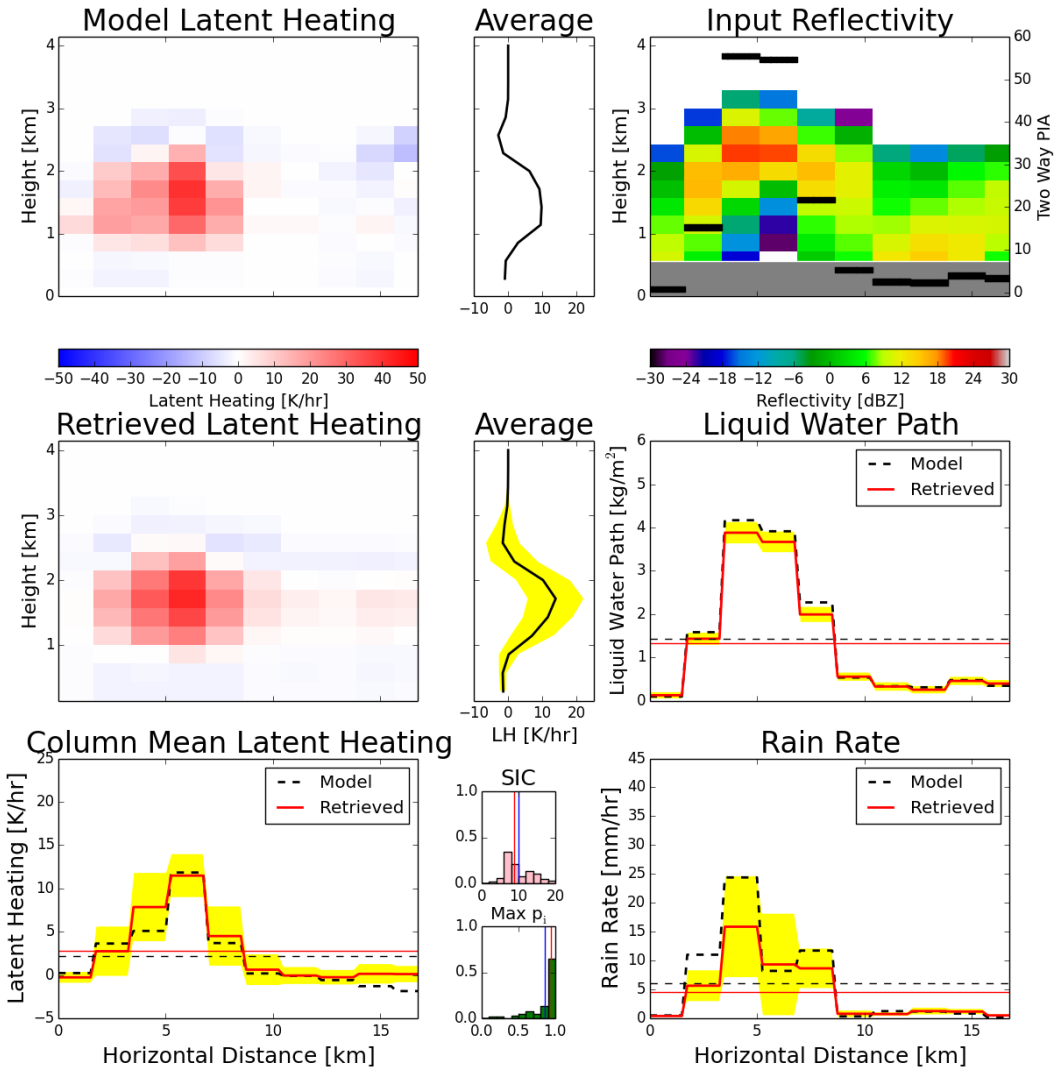

FIGURE 3.5: Same as Figure 3.2, but for CloudSat resolution. Model resolution quantities are also plotted in dotted blue.

3.3.2.1 Example Cross Section

Figure 3.5 repeats the cross section from the previous tests, but with the retrieval degraded to the 1.5 km spatial and 300 m vertical resolution; column mean latent heating, liquid water path, and rain rate from the model resolution are show in dotted blue. Because of the lower resolution, the two cells on the left side have merged into one large area of heating; the dissipating cell on the right side is reduced to an area mostly of upper-level cooling. The average model profile remains nearly the same: a peak in cooling is around 2.2 km, heating is through much of the 1 km to 2 km layer, and slight cooling is below the cloud base. Magnitudes in these areas are very similar, with close to 10 K/hr in the heating core. The reflectivity is missing many of the previous features due to both spatial averaging and the blind curtain in reflectivity up to 550 m. However, the general horseshoe shape of high reflectivities is still discernible on the left side as is the structure on the right side.

The retrieved and average profiles of latent heating in the middle row of the figure show fairly good agreement with the modeled latent heating. The profile with the strongest heating is positioned correctly just past 5 km horizontally. The peak in cooling below the cloud base is retrieved in line with this profile, instead of under the profile just to the left. The peaks in the average profile match that of the model and the uncertainty in the average vertical profile again captures the model profile. Liquid water path

is retrieved nearly exactly, similar to the model resolution performance. Column-averaged latent heating is biased slightly lower, mostly due to under-representation of cooling on the far right side of the cross section. Lastly, the rain rate maximum is matched to the profile left of strongest heating and in the correct position. Regardless of these two pixels, the bias across the cross section is small.

Degrading the resolution does not substantially degrade algorithm performance except at the edges of rain cells where the 0 dBZ threshold can be missed due to the spatial averaging. However, higher resolution features in the scene are obviously smoothed out by the lower resolution observation. This will be further illustrated through comparisons of application of the algorithm to aircraft and satellite observations in Chapter 4.

3.3.2.2 Full Domain Results

The same full model time step degraded to CloudSat resolution is shown in Figure 3.6. Most of the spatial features remain in the degraded resolution. The retrieval picks out the major areas of heating while underestimating cooling on the edges of cells. The spatial pattern of liquid water path is retrieved well in the algorithm results. Rain rate from the algorithm nearly matches the model, with one pixel of very high rain rate missed. Figure 3.7 provides scatter plots between the model and retrieved variables.

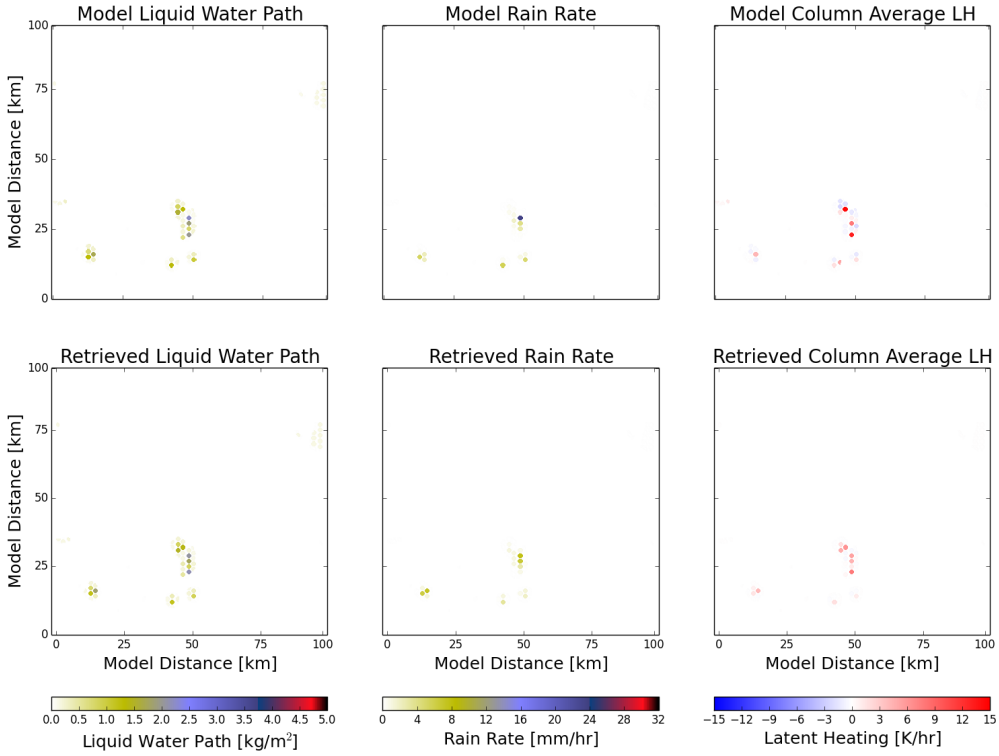

FIGURE 3.6: Same as Figure 3.3, but for the CloudSat resolution retrieval.

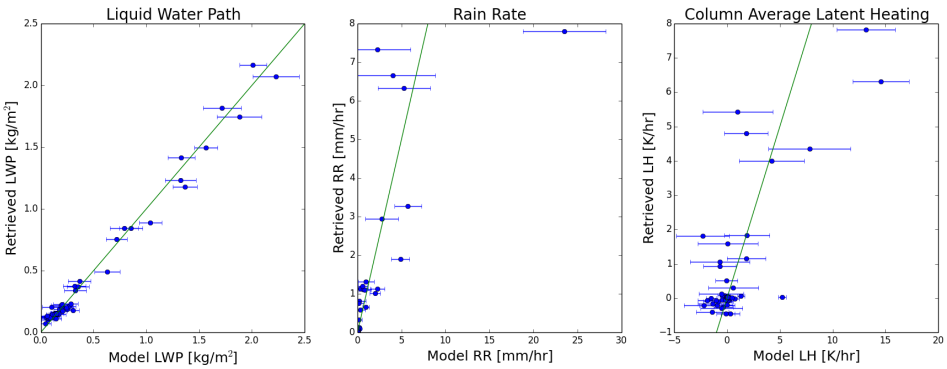

FIGURE 3.7: Same as Figure 3.4, but for CloudSat resolution retrieval.

The relative density of profiles at low column-averaged latent heating values is lower because these are usually associated with profiles that have maximum reflectivities close to 0 dBZ; resolution degradation to CloudSat's specifications causes some of these profiles to no longer reach 0 dBZ after averaging. Nevertheless, LWP continues to follow along the 1:1 ratio between model and retrieval, having a RMSE of 0.068 kg/m^2 and bias of 0.001 kg/m^2 (0.25 %). Rain rate at the CloudSat resolution has a much lower magnitude of RMSE of 2.336 mm/hr and bias at -0.177 mm/hr (-16.27 %); the most intense rain rate pixel is underestimated, likely due to the blind zone, and skews an otherwise nearly 1:1 ratio of rain rate between model and retrieval. Lastly, the latent heating is retrieved well with a RMSE of 1.945 K/hr and bias of 0.031 K/hr (4.59 %).

3.4 Representativeness of Parameters

The effects of removing each of the parameters is examined to qualify the use of each variable and determine the effects of the parameters on the retrieved values. Heights of -30 dBZ and 0 dBZ levels and the near surface reflectivity provide information about the extent of detected rain and cloud vertically. Path integrated reflectivity and two-way path integrated attenuation constrain the intensity of precipitation and amount of water within the column. Removing these groups of variables from the algorithm should cause the retrieval to lose information about these properties. First, the effect of removing the height quantities is examined.

Figure 3.8 shows the cross section retrieval removing the -30 dBZ height from the top, 0 dBZ height from the top, 0 dBZ height from the bottom, and near surface reflectivity. At first glance, the retrieved latent heating profiles are barely constrained vertically. Based on the latent heating structures in Figure 2.5, most of the intense convection in the database has a cloud base near 1 km, signaling the height of the boundary layer. Thus, the algorithm retrieving a cloud base near the truth height despite no vertical information as an input is not new information but rather the result of a database average. The tops of the clouds are ill-defined and situated at either 2 km or 3 km.

All uncertainties have increased dramatically on the quantities. Also, rather than a pronounced transition from heating to cooling vertically, the profile slowly increases in heating from the top of the domain down to about 1.5 km, after which it begins to decrease to slightly below zero at 1 km (again resulting from the database mean). Liquid water path has a low bias, establishing that the integrated parameters provide a good estimate of integrated properties of the cloud. Column mean latent heating is overestimated due to heating over a much larger vertical extent compared to the model and poor retrieval of entrainment cooling at cloud top, especially in regard to the cell on the far right. Rain rate generally follows the same pattern as liquid water path and is biased low.

Next, the complementary set of parameters is used with PIR and two-way PIA instead

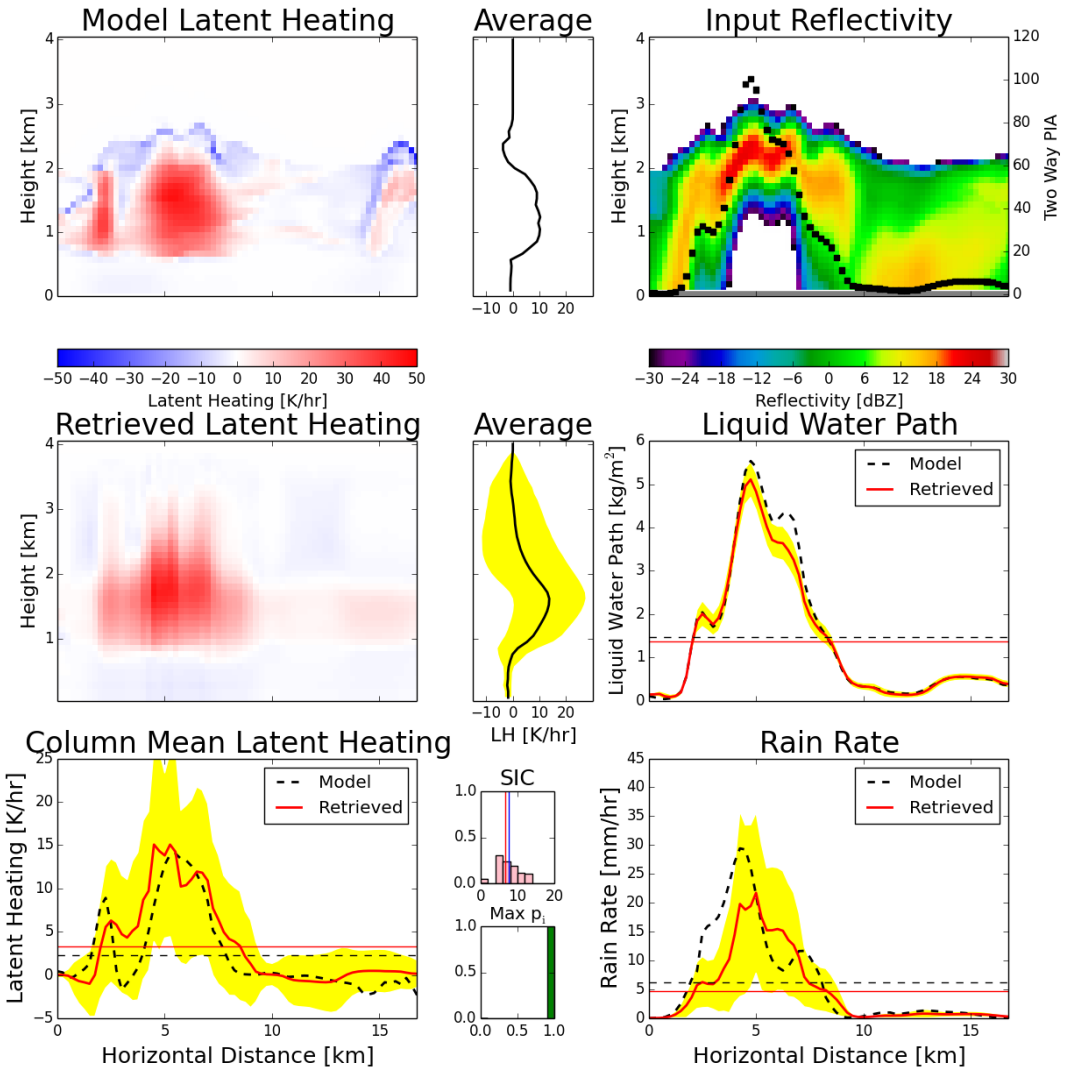

FIGURE 3.8: Same as Figure 3.1 but only using path integrated reflectivity and two-way path integrated attenuation as inputs in the algorithm.

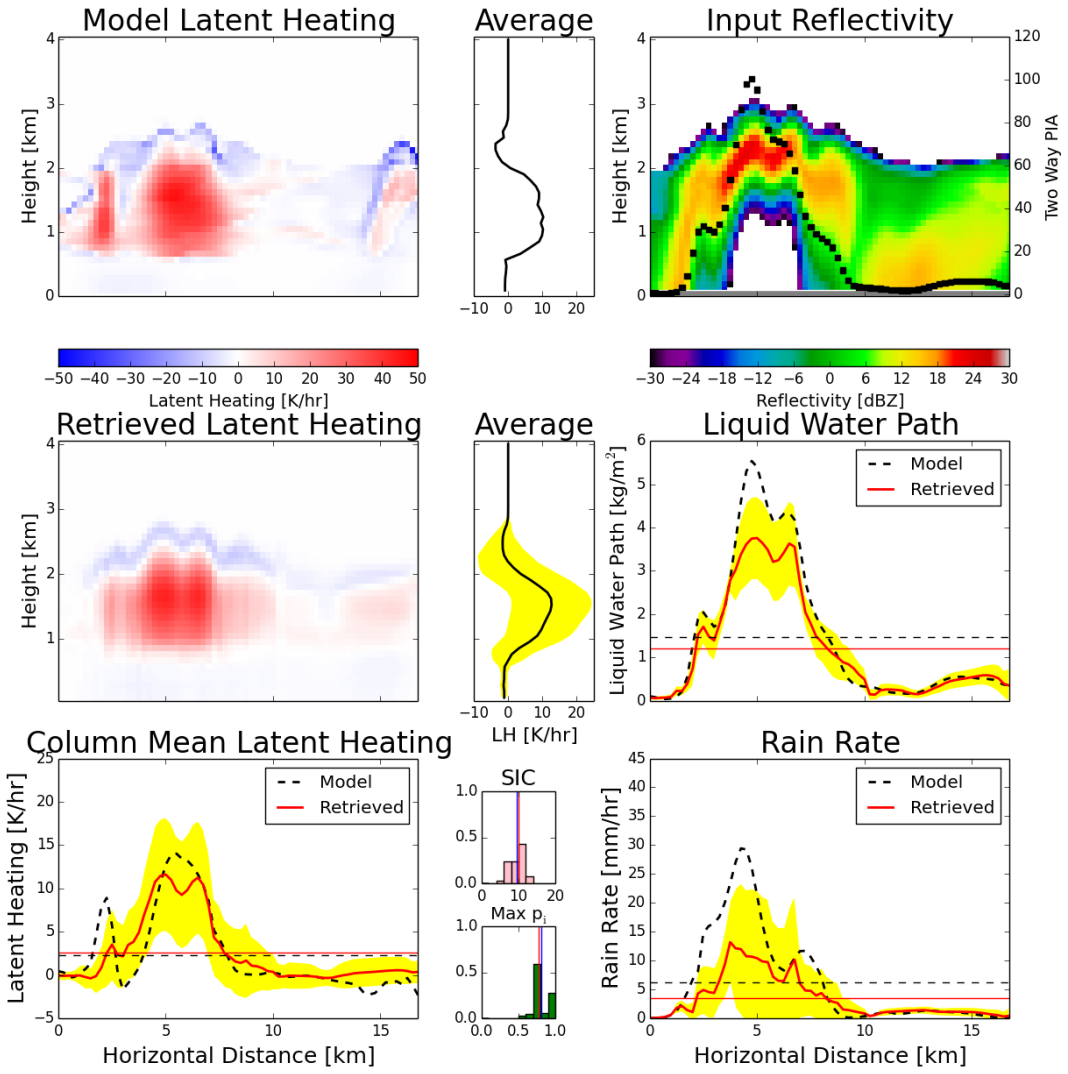

FIGURE 3.9: Same as Figure 3.1 but only using -30 dBZ height from the top, 0 dBZ height from the top, 0 dBZ height from the bottom, and near surface reflectivity.

excluded. Figure 3.9 shows the results of the algorithm application in this case. The vertical structure of the latent heating is retrieved with cloud tops and bases mostly following the model. The cell on the far left of the cross sections fails to be separated from the main cell and the cell on the far right remains mostly connected to the other two. The average latent heating profile is better constrained with no heating or cooling above 3 km and a more marked transition from overall cooling to heating vertically. Liquid water path follows a general structure expected given the retrieved distribution of heating (with liquid water path peaks in the tallest areas of heating), but values are greatly underestimated particularly in regions of full beam attenuation. Column mean latent heating follows the latent heating profiles, while rain rate especially suffers in areas of full beam attenuation.

Retrievals on the same cross section but removing only one parameter at a time are summarized statistically in Table 3.1 and figures of each are included in Appendix A. The most striking difference results from removing two-way PIA: the retrieved liquid water path and rain rate underestimate the model values with rain rate by almost half. PIA serves as a good gauge of the total water in the column and therefore provides estimates of liquid water path and rain rate. Another remarkable difference is removal of the 0 dBZ height from the bottom, which retrieves an erroneous segment of intense rain (nearly double the model values) and does not discern the drop in rainfall near 7 km horizontal distance. This parameter helps to constrain the intensity of precipitation vertically within the cloud as mentioned in the parameter description.

Parameter Removed	LWP [kg/m^2]		RR [mm/hr]		LH [K/hr]	
	RMSE	Bias (%)	RMSE	Bias (%)	RMSE	Bias (%)
Two-way PIA, PIR	0.5427	-0.2598 (-17.67)	2.6744	-2.7363 (-44.20)	2.2628	0.2719 (11.76)
Near surface reflectivity, -30 dBZ height from top, 0 dBZ height from top, and 0 dBZ height from bottom	0.2576	-0.1027 (-6.99)	2.1015	-1.4359 (-23.19)	2.6036	1.0212 (44.15)
Two-way PIA	0.4707	-0.1835 (-12.48)	2.6386	-2.2445 (-36.25)	2.1028	0.256 (11.07)
PIR	0.2489	-0.0908 (-6.18)	1.2882	-1.0875 (-17.57)	2.5368	0.2640 (11.41)
Near surface reflectivity	0.2523	-0.1162 (-7.90)	1.3838	-1.3202 (-21.32)	2.4196	0.1383 (5.98)
-30 dBZ height from top	0.2539	-0.1202 (-8.18)	1.2198	-0.9922 (-16.03)	2.1935	0.2595 (11.22)
0 dBZ height from top	0.2471	-0.1211 (-8.24)	1.2179	-1.059 (-17.11)	2.3567	0.2258 (9.76)
0 dBZ height from bottom	0.2796	-0.1266 (-8.61)	1.629	-0.4758 (-7.69)	2.5264	-0.0039 (-0.17)
Original configuration	0.2513	-0.1191 (-8.10)	1.2394	-1.2021 (-19.41)	2.4072	0.0955 (4.13)

TABLE 3.1: Table of statistics for parameter removal tests on the cross section in Figure 2.6.

3.5 Environmental Conditions and Information

3.5.1 Deducing Environmental Conditions

Given the systematic differences in the character of reflectivity and latent heating in model runs with distinct SST and CCNC, it is interesting to ask whether characteristics of the reflectivity profile can provide information about the stability of the environment and possibly also the aerosol conditions. More unstable environments yield clouds that are more expansive and vigorous in convection, while more stable environments exhibit capped and stratiform-type clouds. Furthermore, with insights from the aerosol indirect effect sensitivities, the presence of fewer aerosols in unstable environments should promote accelerated growth of water droplets compared to those with more aerosols leading to higher precipitation yields for a given liquid water path. Several of these principles may be represented in the profile characteristics used in the algorithm.

To test the extent to which the algorithm can distinguish aspects of the environment in which precipitation forms, two profiles are randomly picked out of a time step not included in the database: one from the 293 K 400 cc run and another from the 303 K 800 cc run. Figure 3.10 shows on the left the vertical reflectivity profile and two-way path integrated attenuation for the first case and the corresponding histogram of the total probability from all profiles in each simulation is on the right; surface rainfall rate is 0.02 mm/hr. Profiles from the simulation with CCNC and SST that match this

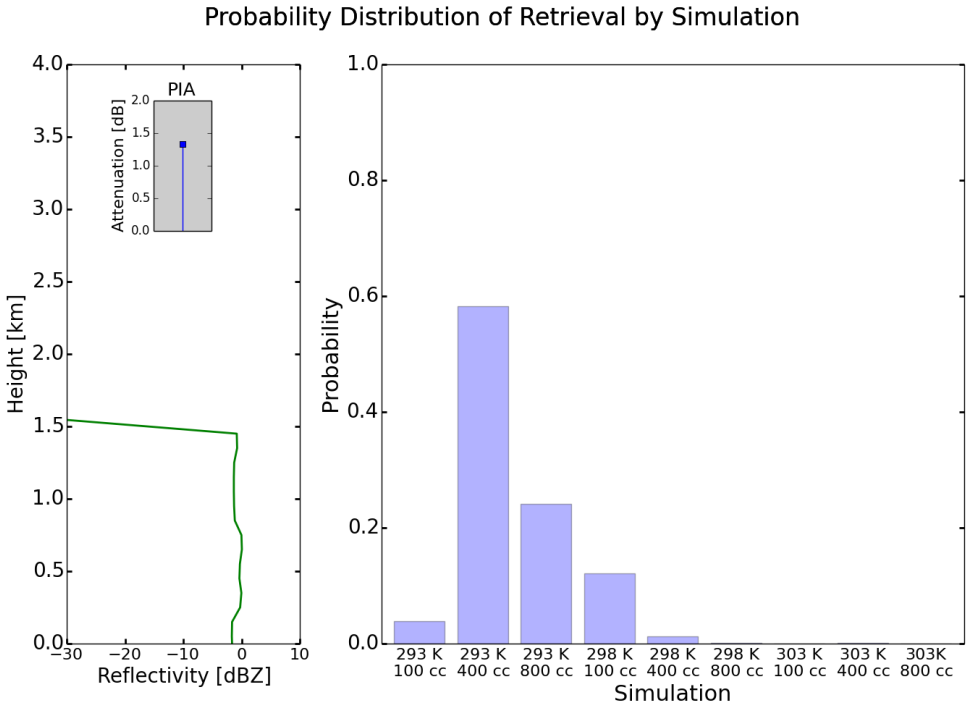

FIGURE 3.10: Sample profile from the 293 K 400 cc model run and the corresponding retrieval total probabilities by simulation.

profile has are sampled almost three times more frequently than any other simulation in the database. The second highest probability corresponds to the 293 K 800 cc case. More than 90% of the profile weights that enter the retrieval come from profiles with an SST of 293 K, suggesting that the retrieval parameters correctly identify that this scene developed under stable conditions.

Similar results for a profile from the 303 K 800 cc run with a surface rain rate of 4.6 mm/hr are shown in Figure 3.11. The run matching the conditions of this profile contributes the largest probability to the retrieval, totaling 0.51. Although the retrieval incorporates profiles from several different sets of environmental conditions, all

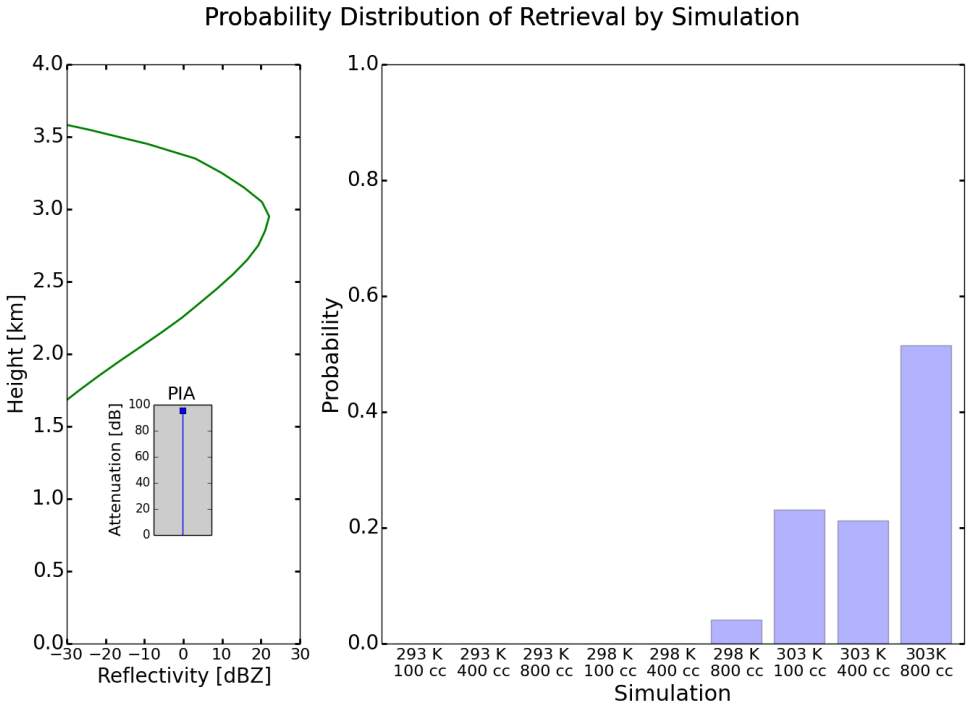

FIGURE 3.11: Sample profile from the 303 K 800 cc model run and the corresponding retrieval total probabilities by simulation.

other simulations combined contribute less than 25% to the retrieval with the other two largest probabilities from a similar stability regime. This lends some credence to the ability to generally determine the stability of the environment by examining the structure and magnitude of the reflectivity profile.

3.5.2 Adding Environmental Information

The algorithm can generally pick out the local thermodynamic stability regime of a profile, but the aerosol levels in the environment are not so surely determined. Each level of aerosol contains a spectrum of precipitation states that together populate the database, so there is some overlap between states from the different simulations. For

example, a moderate rainfall profile of the high aerosol case may be similar to a strong rainfall profile of the lower aerosol case; each simulation is not wholly unique from the others. Providing information about the aerosol environment, therefore, may further constrain some of the retrieved quantities.

An aerosol measurement of the environment is included in the same retrieval as Section 3.3.1.1 with an error of 100 cc. The distribution of latent heating is nearly the same, with a few profiles intensifying within the core. The level of peak heating in the average vertical profile remains the same but the quantity is decreased while the profile below that peak slightly intensifies; in other words, the bottom-heaviness of the profile slightly increased. This is expected as, from before, isolated systems have a latent heating profile that peaks closer to the ground. Recalling Figure 2.3, the aerosol concentration has a notable effect on the precipitation efficiency for a given liquid water path. As the liquid water path is better constrained with the addition of aerosol information (the bias in this case is 5.81 % compared to -8.10 % in the original algorithm), the rain rate estimate is also improved (a bias of -12.2 % compared to -19.41 % before). Ergo, the addition of an aerosol observation may in fact better constrain the retrieval of the algorithm in line with the expected effects caused by the aerosol indirect effects.

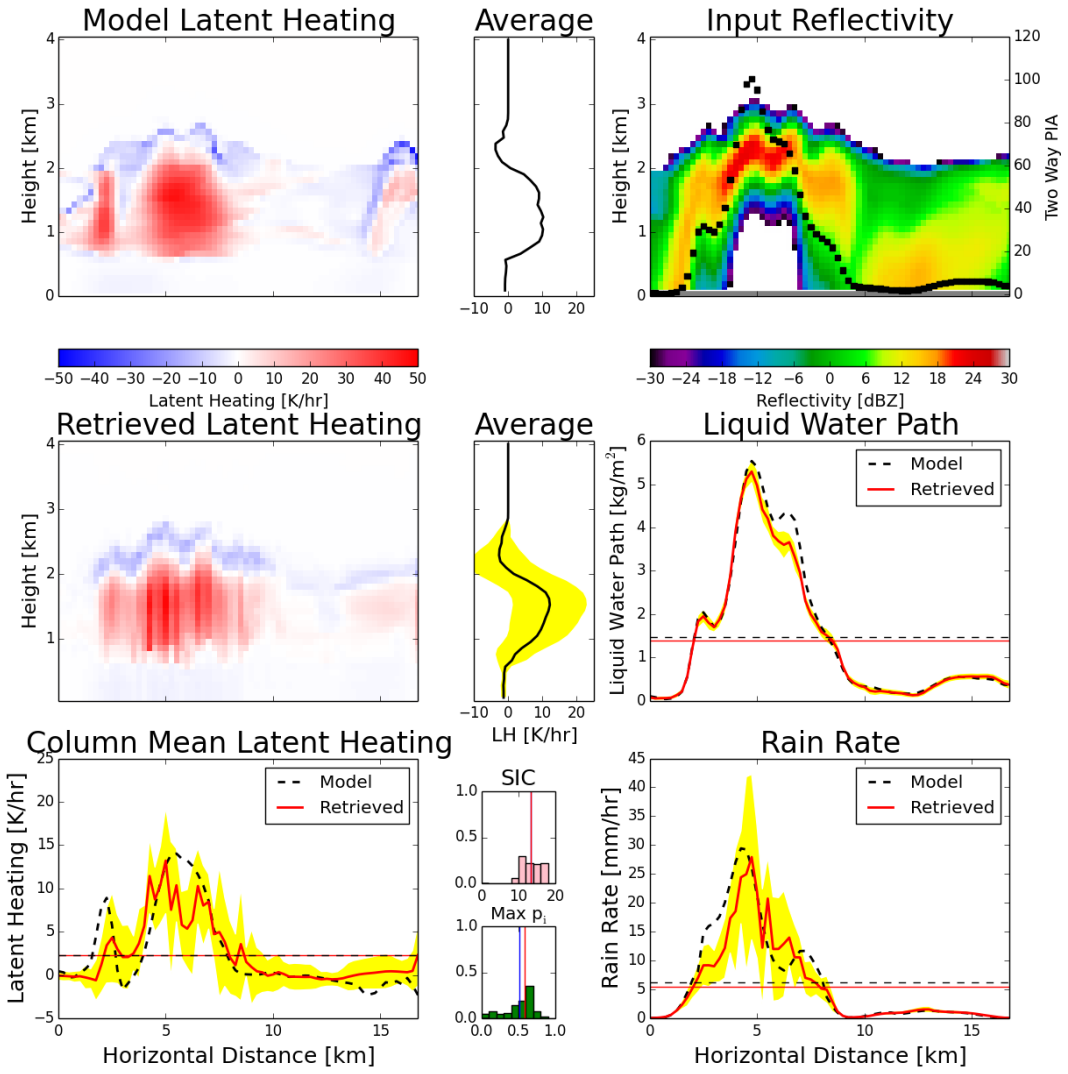

FIGURE 3.12: Same as Figure 3.2 but including an aerosol measurement with an error of 100 cc.

Chapter 4

Observation Analyses

4.1 VOCALS Field Experiment Estimates

The VAMOS Ocean-Cloud-Atmosphere-Land Study, or VOCALS, is an international study to determine the mechanisms and effects of aerosol indirect effects in the Southeastern Pacific Ocean and to improve atmospheric and coupled atmosphere-ocean models in this area (Mechoso et al., 2014). One part of the VOCALS program is a field campaign called the VOCALS-Regional Experiment (VOCALS-REX). VOCALS-REX was composed of intensive observations of ship-based, aerial, and land-based observations including radar, radiosonde, and aerosol measurements.

One of the participating aircraft was the NSF/NCAR C-130 equipped with the Wyoming Cloud Radar, a 94 GHz (W-band) radar. On October 28, 2008, the aircraft flew

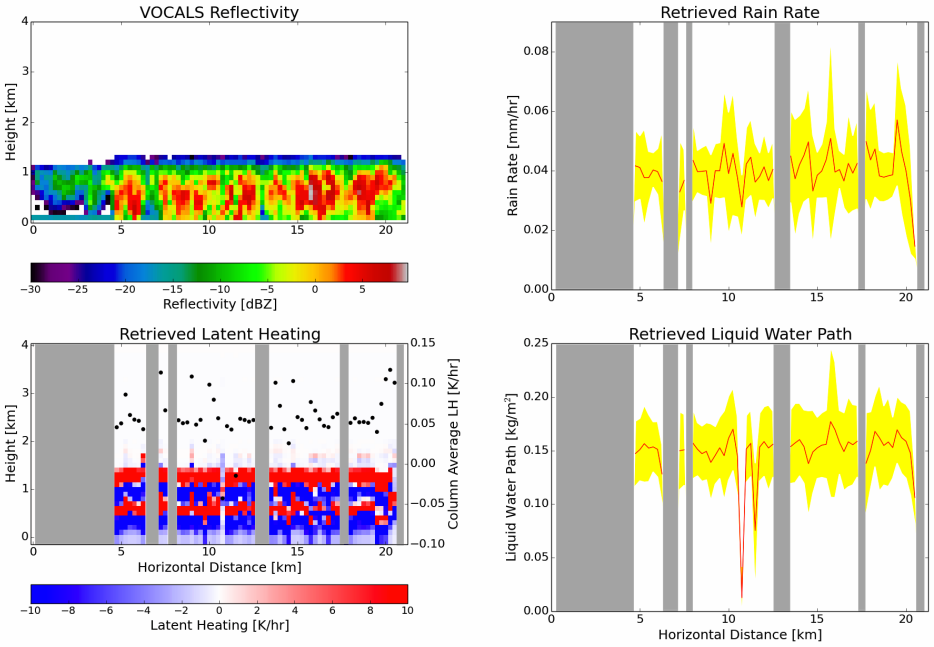

FIGURE 4.1: Retrievals of VOCALS C-130 W-band aircraft-based reflectivity, taken on October 28, 2008 at 9 UTC. Counterclockwise from the top left displayed are reflectivity, retrieved vertical profiles and column-averaged latent heating, retrieved liquid water path, and retrieved rain rate of the scene. Data courtesy of L. Ooolman and D. Leon (U. Wyoming).

through large marine boundary layer clouds. The top left of Figure 4.1 displays the reflectivity upscaled to the model resolution of the algorithm; no attenuation information was available. Areas where the reflectivity profiles do not reach 0 dBZ are masked in gray. A capped cloud layer is present in the scene with pockets of enhanced precipitation. The retrieval generates a general heating trend over the region, with higher levels of rain and liquid water path corresponding to higher column-averaged latent heating. For most of the retrieved scene, rain rates are on the order of 0.04 mm/hr and liquid water path 0.15 kg/m^2.

4.2 CloudSat Granule Estimates

Next, a CloudSat granule is examined in the context of the algorithm, since it is designed for CloudSat. A shallow tropical raining scene is selected from Granule #18422, which passed over the Southeastern Pacific Ocean on October 14, 2009. The top panels of Figure 4.2 show the reflectivity structure, attenuation, and location of the overpass. Reflectivities are taken directly from the 2B-GEOPROF product with noise above the scene removed. Attenuation values are chosen to be the two-way, near surface bin attenuation from 2C-PRECIP-COLUMN.

The second row of plots displays the retrieved vertical profiles of latent heating, overlaid with each profile's column-averaged latent heating, and the swath's average vertical profile of latent heating. Areas masked out in gray are due to a profile either not reaching the 0 dBZ threshold or falling outside of the database range. The largest contributor to the latter is a vertical extent that greatly exceeds the 4 km algorithm top; these will likely be retrievable once the database is expanded to include shallow convection in large-scale radiative-convective equilibrium simulations from the archive of RAMS simulations (see Chapter 6).

Through the extent of the swath, areas of strong reflectivity and precipitation reaching the bottom bin coincide with high rain rates (with a maximum of 4 mm/hr) and high liquid water paths. The spatial pattern of latent heating is consistent with physical expectations; heating is strongest in areas that the reflectivity is greatest and the taller

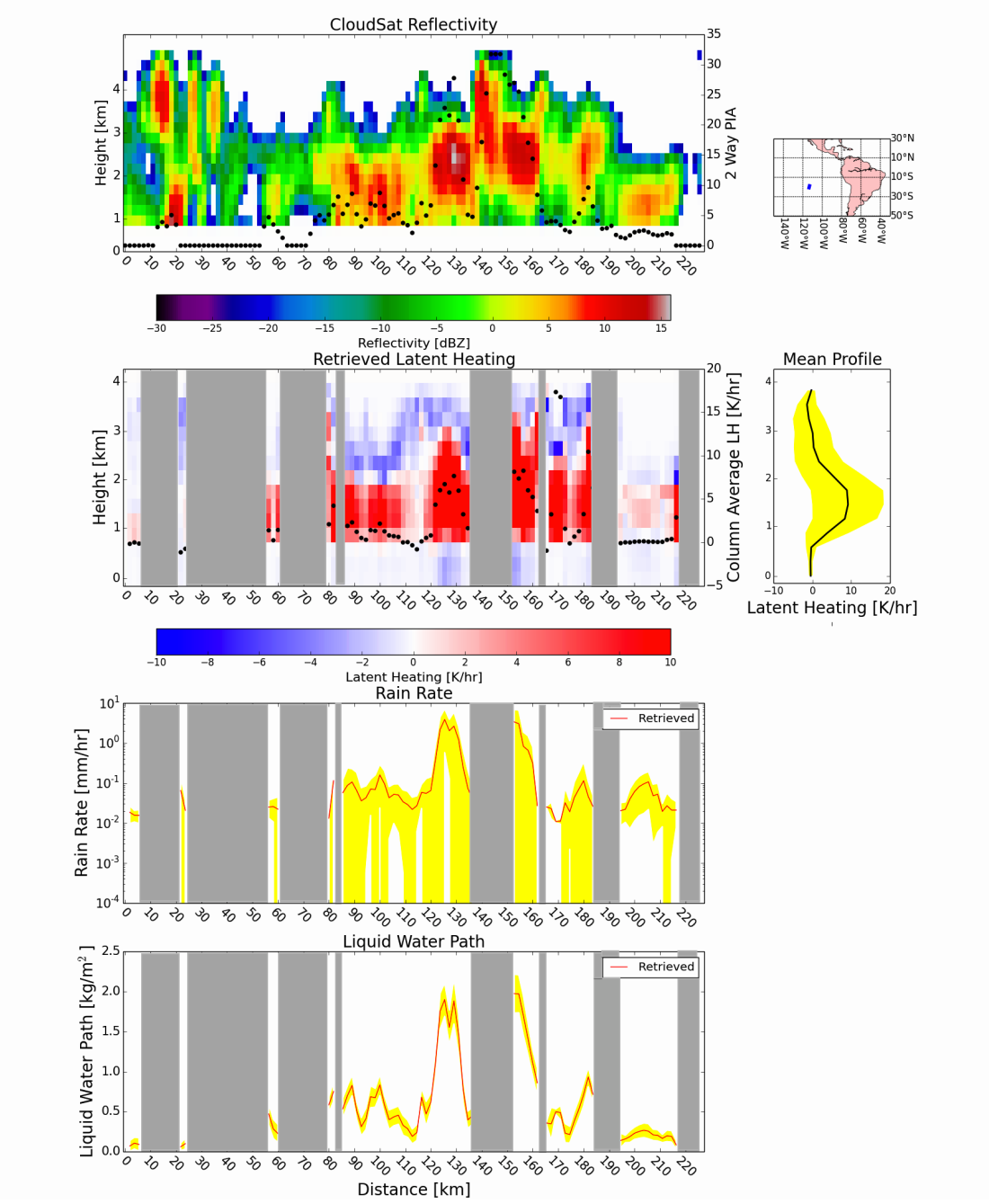

FIGURE 4.2: Retrieval on CloudSat granule #18422, passing over the Southeastern Pacific Ocean on October 14, 2009. The top left plot shows the vertical reflectivity structure and two-way path integrated attenuation; the top right image is a map of the scene with respect to the surrounding area. The second row left plot displays the retrieved vertical structure of latent heating and overlaid is the column-averaged latent heating; the second right plot is a swath-averaged vertical latent heating profile. The bottom two plots are the retrieved rain rates and liquid water paths. Data courtesy of the CloudSat Data Processing Center.

cores coincide with the retrieved latent heating vertical structure. Cooling occurs at the cloud top due to entrainment of drier air. Strong cooling also exists below the cloud base in areas that the surface rain rate is greater than 2 mm/hr.

Chapter 5

Conclusion

5.1 Algorithm Performance

In answering the study objective, the algorithm successfully retrieved the latent heating structure of the cross sections and domains in the synthetic retrievals. Table 5.1 highlights the error statistics of the model and CloudSat resolution synthetic domain runs. At model resolution, biases remained low despite higher root mean square errors, an indication that across the domain errors canceled out. Degrading the algorithm to CloudSat resolution proved to show similar results, with LWP and rain rate biases remaining on the same order as model resolution. Beyond averaging, differences also arose between the two due to the blind zone of reflectivity with CloudSat. Reflectivities below 550 m were not included as this approximate height is designated as the

	LH [K/hr]		LWP [kg/m^2]		RR [mm/hr]	
Resolution	Bias	RMSE	Bias	RMSE	Bias	RMSE
Model	0.080	2.975	0.008	0.079	-0.227	1.902
CloudSat	0.031	1.945	0.001	0.068	-0.177	2.336

TABLE 5.1: Table displaying the statistical results of the synthetic domain analyses.

lowest non-affected bin from surface reflection.

Choosing to use parameters that describe the cloud structure and intensity instead of the full reflectivity for the profile was shown to be both advantageous and proper for the database construction. The physical dependence of the retrieval on each of the parameters was shown by examining the effects of removing each one individually, as well as the bulk classifications of the integrated and vertical quantities. Insights from the aerosol indirect effects proved to help further constrain liquid water path and in turn rainfall rate when including an environmental aerosol measurement in the algorithm. Additionally, the ability to estimate stability characteristics of a profile might be possible as the parameters used in the algorithm discern the extent and intensity of clouds. Two randomly selected profiles from different simulations successfully showed this.

Retrievals on real observations, both from field campaigns and CloudSat, provided realistic structures of latent heating and quantities of rainfall and liquid water path. The flexibility of this algorithm's application to any radar platform was therefore demonstrated. The most intense areas of heating embedded within the CloudSat swath in Figure 4.2 of clouds ranged from a horizontal size of 2 km to 10 km. The lower

end of this range is less than the the swath size of previous satellite radar missions. Further, the greatest reflectivity detected is about 15 dBZ. Thus, the algorithm is able to provide an estimate of precipitation regimes not previously possible.

The selection of a Bayesian framework for the algorithm provides the flexibility for it to be used with other observing platforms. Frequencies of radar observations can be altered to suit different instruments if needed. This leads to the future work to extend and expand this project detailed in the next chapter.

Chapter 6

Future Work

6.1 Error Analysis

The errors assumed in the calculations for this algorithm were based solely on the current instrument uncertainties. Moreover, no correlations between different variables were included. An algorithm that takes into account the variances and covariances of all the variables provides the best posterior distribution. Rigorous error analysis will be performed on the algorithm by propagating random noise through the database to determine the effect on the algorithm results. Dependencies between variables to fill in the off-diagonals of the covariance matrix will be calculated.

6.2 Composite Analysis of the MJO

As noted at the outset, one of the primary problems motivating this work is the reported lack of reliable estimates of a shallow latent heating mode in TRMM-based analyses of the MJO (Jiang et al., 2011). The algorithm can be used to observationally explore the incipient stages of the Madden-Julian Oscillation. Beginning condensation in the lower areas of the atmosphere serves as a destabilizer of the environment to prime for the later phases of MJO progression. Despite the significance of the initial heating, this stage of the MJO has been largely underrepresented in latent heating observations derived from previously latent heating algorithms. Once this algorithm has been applied to the complete CloudSat record, the resulting CloudSat-based latent heating product can be used to perform composite analyses on the effects of shallow convection on the strength and progression of the MJO.

6.3 Database Expansion

An exhaustive archive of different RAMS simulations exists spanning a wide array of precipitation types, from tropical and extratropical cyclones to stratiform rain events. Following the same process that was used to establish this algorithm, these simulations can be processed to create new databases. Implementing a radar simulator that models mixed phase and frozen precipitation will provide simulations of reflectivity closer to that actually observed. The expanded algorithm could potentially use

environmental conditions derived from the National Centers for Environmental Prediction's Global Forecast System or the European Centre for Medium-Range Weather Forecasts' Integrated Forecast System to determine the simulation-derived database most appropriate for the observations, providing a robust algorithm for latent heating from CloudSat.

6.4 Global Analyses of Latent Heating

Once the database has been expanded to span the spectrum of precipitation regimes, the full algorithm will be run on the complete CloudSat archive of data to create a new data product to coincide with the current CloudSat data products. Global analyses will be performed on the spatial and temporal distributions of latent heating leveraging CloudSat's location on the A-Train, with an orbit that extends into the extratropical and subpolar regions. Moreover, the potential to combine CloudSat's lighter precipitation detection with TRMM's heavier precipitation detection gives way to a more complete perspective of latent heating within the tropical regions of the atmosphere.

6.5 Satellite Design

Using information content metrics, the configuration of hypothetical satellite instruments can be tested to determine the necessary radar and orbit characteristics needed to better constrain latent heating. Such features include the footprint size of the radar,

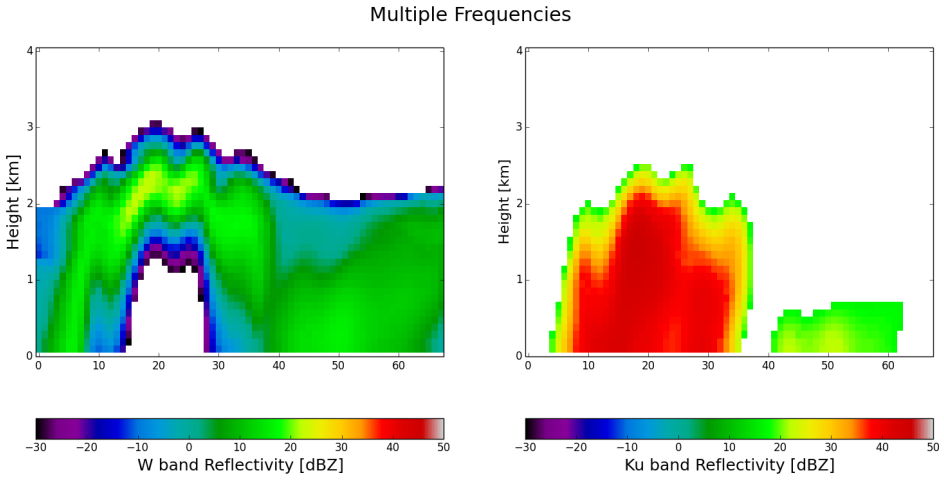

FIGURE 6.1: Same scene from Figure 2.6 with both the 94 GHz (W band) and 13.6 GHz (Ku band) reflectivities, simulating a synergy of complementary CloudSat CPR and TRMM PR perspectives.

radar resolution, and the angle of the satellite beam. Moreover, multiple frequencies can be added to the algorithm along with Doppler velocities. Figure 6.1 shows the potential value in adding more than one frequency observation of a given reflectivity scene. Higher frequencies become attenuated but can detect the lighter features of clouds, while lower frequencies cannot see the areas of lower water content but can detect the denser parts of clouds without the signal attenuating fully. Evaluations of proposed future satellite missions can therefore be completed with the aid of the full algorithm framework.

Appendix A

Parameter Representativeness Continued

From Section 3.4, the following are retrievals on the same cross section as Figure 3.1 removing only a single parameter at a time. Table 3.1 displays the associated statistics with each trial.

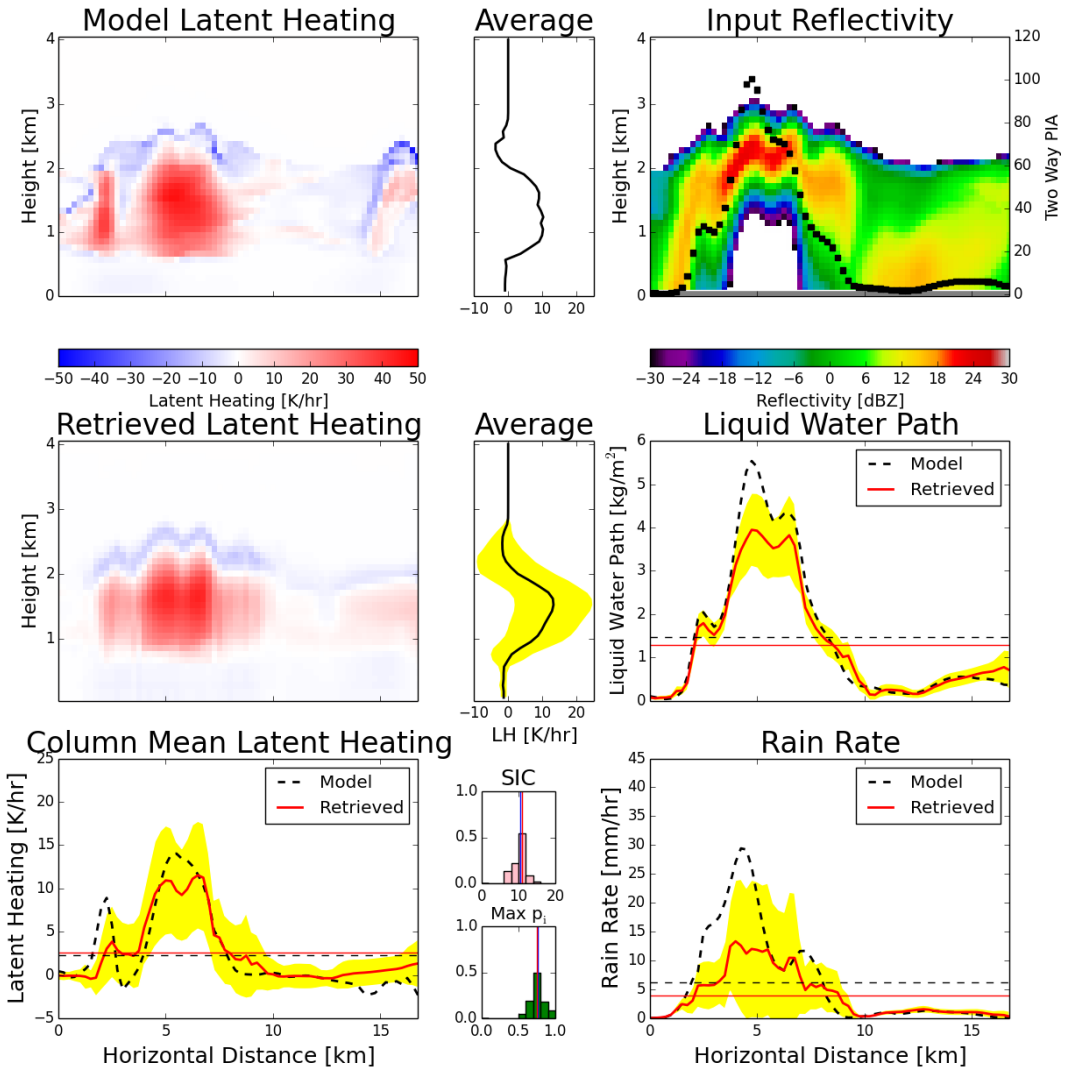

FIGURE A.1: Same as Figure 3.1, but using the algorithm parameters except the two-way PIA.

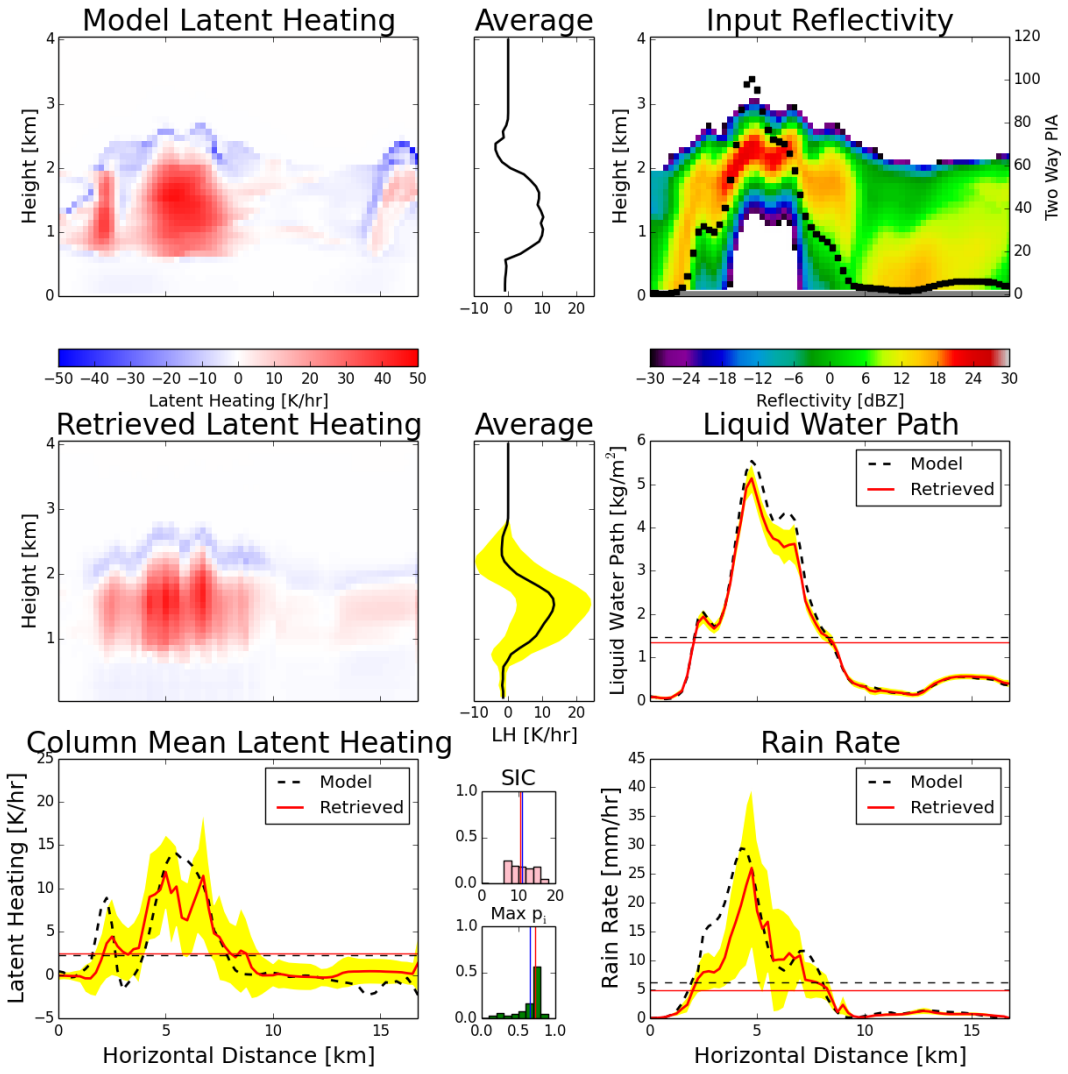

FIGURE A.2: Same as Figure 3.1, but using the algorithm parameters except the near surface reflectivity.

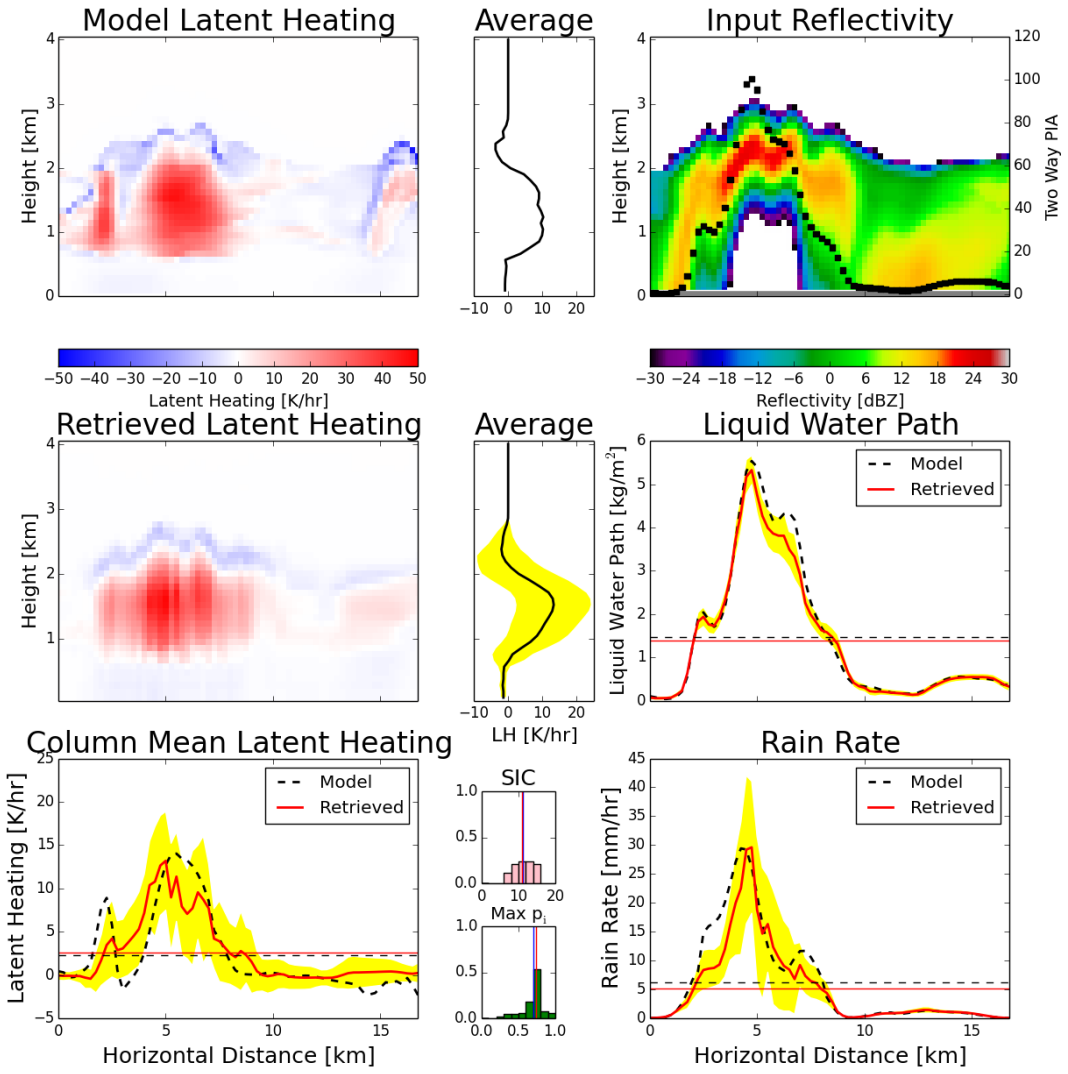

FIGURE A.3: Same as Figure 3.1, but using the algorithm parameters except the PIR.

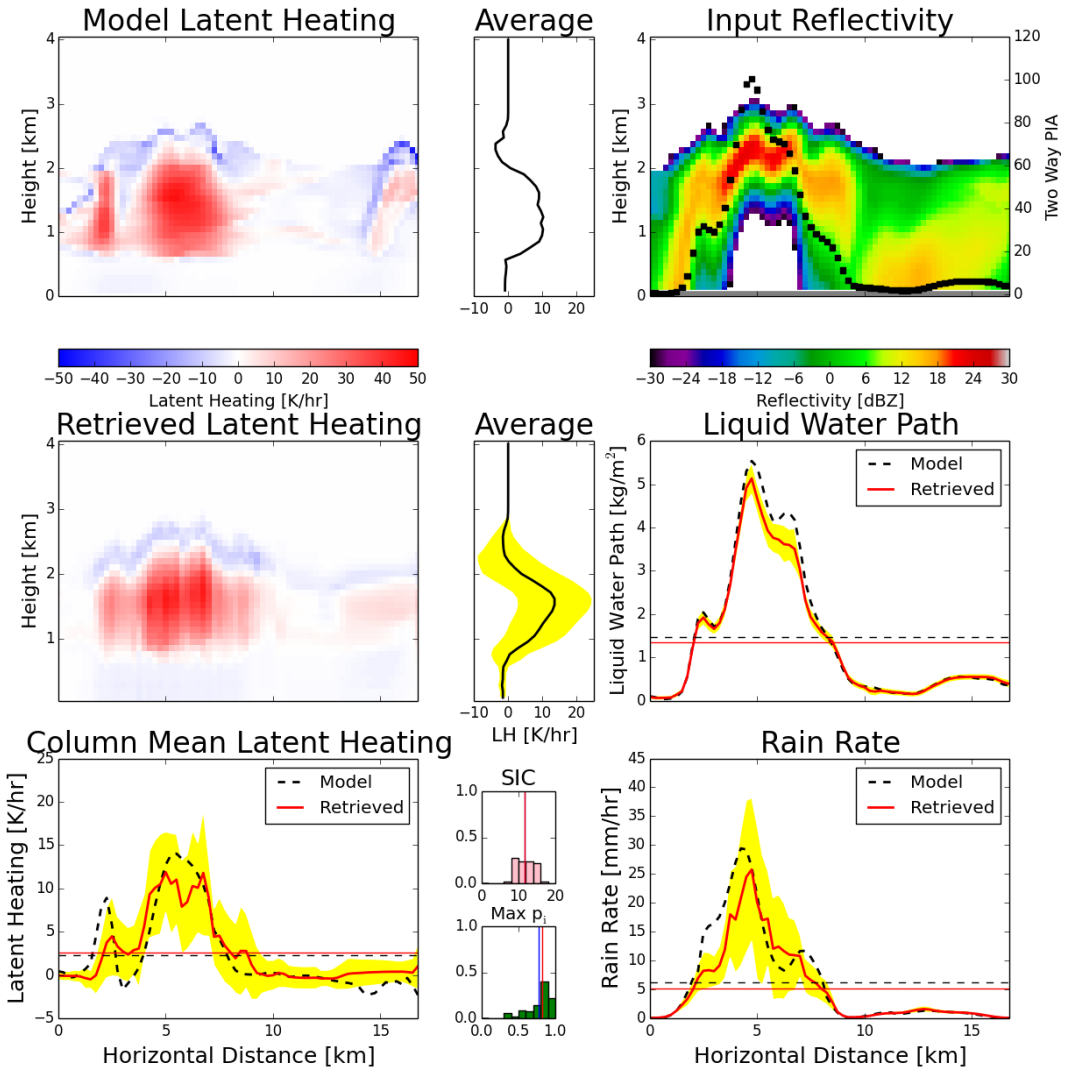

FIGURE A.4: Same as Figure 3.1, but using the algorithm parameters except the -30 dBZ height from the top.

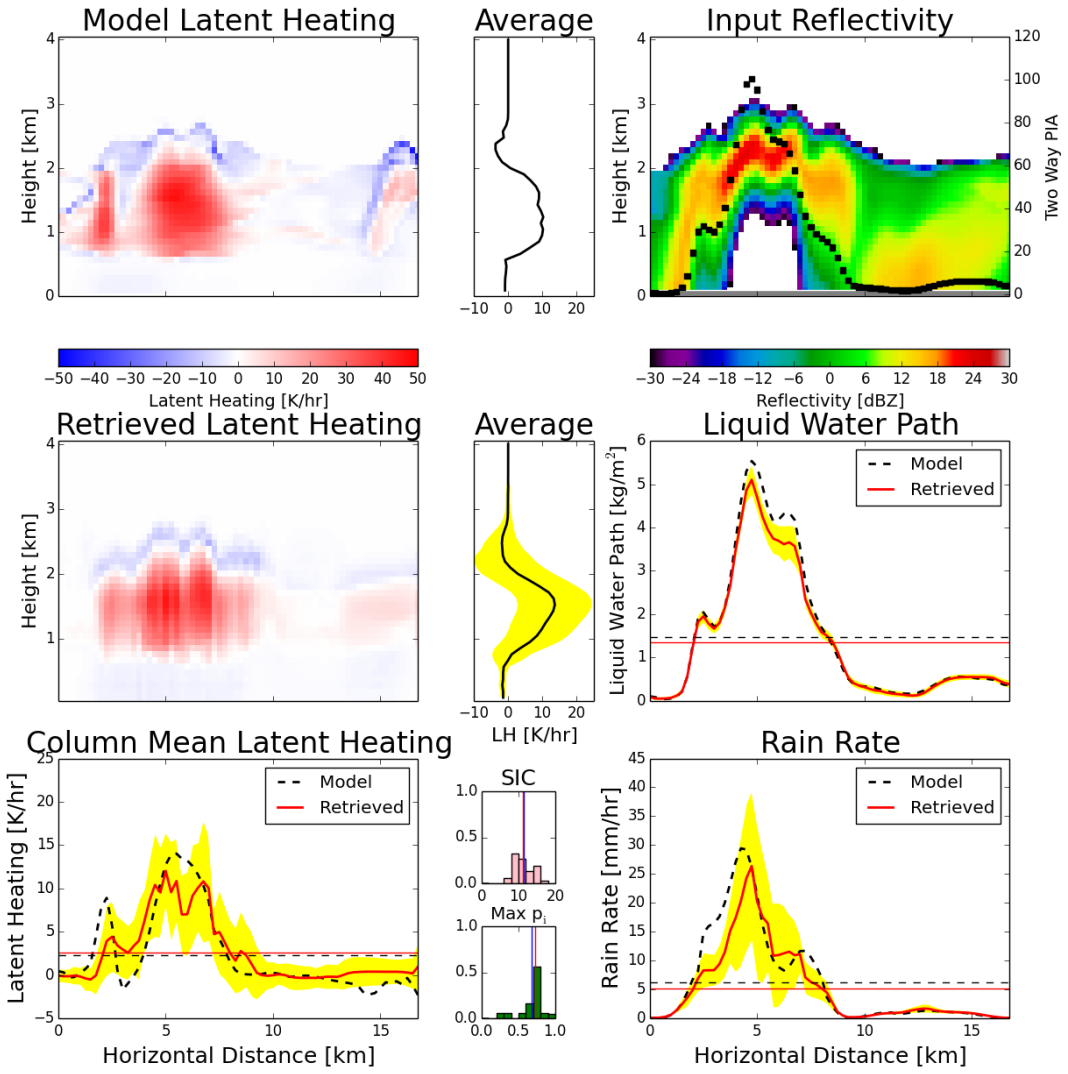

FIGURE A.5: Same as Figure 3.1, but using the algorithm parameters except the 0 dBZ height from the top.

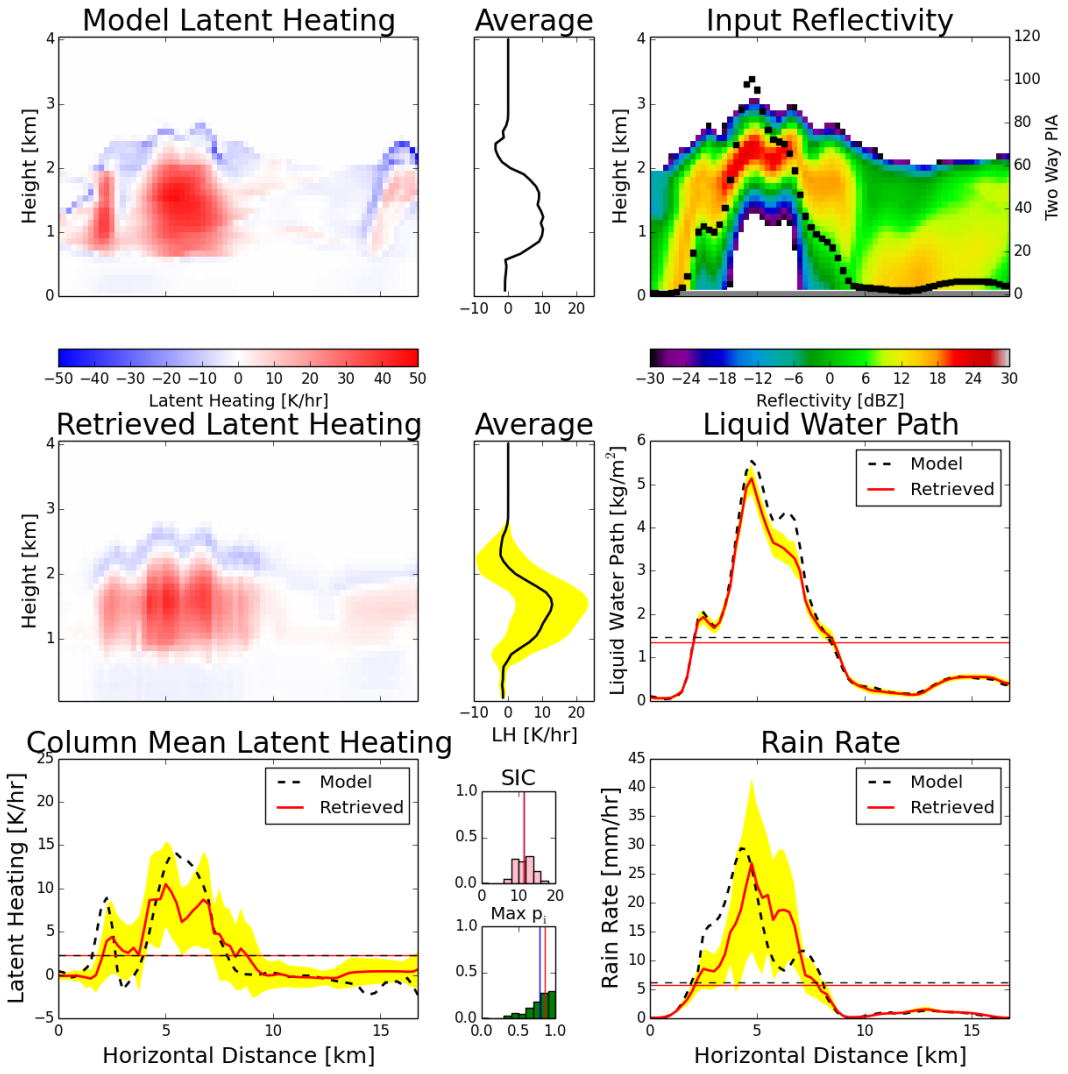

FIGURE A.6: Same as Figure 3.1, but using the algorithm parameters except the 0 dBZ height from the bottom.

Bibliography

Anthes, R. A. and D. Keyser, 1979: Tests of a Fine-Mesh Model over Europe and the United States. *Monthly Weather Review*, **107 (8)**, 963–984, doi:10.1175/1520-0493(1979)107⟨0963:TOAFMM⟩2.0.CO;2.

Aubert, E. J., 1957: On the release of latent heat as a factor in large scale atmospheric motions. *Journal of Meteorology*, **14 (6)**, 527–542, doi:10.1175/1520-0469(1957)014⟨0527:OTROLH⟩2.0.CO;2.

Augstein, E., H. Riehl, F. Ostapoff, and V. Wagner, 1973: Mass and Energy Transports in an Undisturbed Atlantic Trade-Wind Flow. *Monthly Weather Review*, **101 (2)**, 101–111, doi:10.1175/1520-0493(1973)101⟨0101:MAETIA⟩2.3.CO;2.

Augstein, E., H. Schmidt, and F. Ostapoff, 1974: The vertical structure of the atmospheric planetary boundary layer in undisturbed trade winds over the Atlantic Ocean. *Boundary-Layer Meteorology*, **6 (1-2)**, doi:10.1007/BF00232480.

Berg, W., T. L'Ecuyer, and J. M. Haynes, 2010: The Distribution of Rainfall over Oceans from Spaceborne Radars. *Journal of Applied Meteorology and Climatology*, **49 (3)**, 535–543, doi:10.1175/2009JAMC2330.1.

Black, J., 1770: An enquiry into the general effects of heat. *Eighteenth Century Collections Online*, URL `http://find.galegroup.com/ecco/infomark.do?&source=gale&prodId=ECCO&tabID=T001&docId=CB127301258&type=multipage&contentSet=ECCOArticles&version=1.0&docLevel=FASCIMILE`.

Cotton, W. R., et al., 2003: RAMS 2001: Current status and future directions. *Meteorology and Atmospheric Physics*, **82 (1-4)**, 5–29, doi:10.1007/s00703-001-0584-9.

Evans, K. F., J. Turk, T. Wong, and G. L. Stephens, 1995: A Bayesian Approach to Microwave Precipitation Profile Retrieval. *Journal of Applied Meteorology*, **34**, 260–279, doi:10.1175/1520-0450(1995)034⟨0260:ABATMP⟩2.0.CO;2.

Handlos, Z. J. and L. E. Back, 2014: Estimating Vertical Motion Profile Shape within Tropical Weather States over the Oceans. *Journal of Climate*, **27 (20)**, 7667–7686, doi:10.1175/JCLI-D-13-00602.1.

Hartmann, D. L., H. H. Hendon, and R. A. Houze, 1984: Some Implications of the Mesoscale Circulations in Tropical Cloud Clusters for Large-Scale Dynamics and Climate. *Journal of the Atmospheric Sciences*, **41 (1)**, 113–121, doi:10.1175/1520-0469(1984)041⟨0113:SIOTMC⟩2.0.CO;2.

Haynes, J. M., T. S. L'Ecuyer, G. L. Stephens, S. D. Miller, C. Mitrescu, N. B. Wood, and S. Tanelli, 2009: Rainfall retrieval over the ocean with spaceborne W-band radar. *Journal of Geophysical Research*, **114**, D00A22, doi:10.1029/2008JD009973.

Haynes, J. M., Z. Luo, G. L. Stephens, R. T. Marchand, and A. Bodas-Salcedo, 2010: A Multipurpose Radar Simulation Package: QuickBeam. doi:10.1175/BAMS-88-11-1723.

Herbener, S. R., S. M. Saleeby, S. C. van den Heever, and T. S. L'Ecuyer, 2014: Influences of aerosols and ocean temperature on the optical thickness of stratocumulus clouds. *Journal of the Atmospheric Sciences*, In review.

Higgins, W. and D. Gochis, 2007: Synthesis of Results from the North American Monsoon Experiment (NAME) Process Study. *Journal of Climate*, **20 (9)**, 1601–1607, doi:10.1175/JCLI4081.1.

Houze, J., R. A., 1982: Cloud clusters and large-scale vertical motions in the Tropics. *Journal of the Meteorological Society of Japan*, **(60)**, 396–410.

Jiang, X., et al., 2011: Vertical Diabatic Heating Structure of the MJO: Intercomparison between Recent Reanalyses and TRMM Estimates. *Monthly Weather Review*, **139 (10)**, 3208–3223, doi:10.1175/2011MWR3636.1.

Johnson, R. H., T. M. Rickenbach, S. A. Rutledge, P. E. Ciesielski, and W. H. Schubert, 1999: Trimodal Characteristics of Tropical Convection. *Journal of Climate*, **12 (8)**, 2397–2418, doi:10.1175/1520-0442(1999)012⟨2397:TCOTC⟩2.0.CO;2.

L'Ecuyer, T. S., P. Gabriel, K. Leesman, S. J. Cooper, and G. L. Stephens, 2006: Objective Assessment of the Information Content of Visible and Infrared Radiance Measurements for Cloud Microphysical Property Retrievals over the Global Oceans. Part I: Liquid Clouds. *Journal of Applied Meteorology and Climatology*, **45 (1)**, 20–41, doi:10.1175/JAM2326.1.

L'Ecuyer, T. S. and G. L. Stephens, 2002: An uncertainty model for Bayesian Monte Carlo retrieval algorithms: Application to the TRMM observing system. *Quarterly Journal of the Royal Meteorological Society*, **128 (583)**, 1713–1737, doi:10.1002/qj.200212858316.

Martin, J. E. and J. A. Otkin, 2004: The Rapid Growth and Decay of an Extratropical Cyclone over the Central Pacific Ocean. *Weather and Forecasting*, **19 (2)**, 358–376, doi:10.1175/1520-0434(2004)019⟨0358:TRGADO⟩2.0.CO;2.

Mechoso, C. R., et al., 2014: Ocean-Cloud-Atmosphere-Land Interactions in the Southeastern Pacific: The VOCALS Program. *Bulletin of the American Meteorological Society*, **95 (3)**, 357–375, doi:10.1175/BAMS-D-11-00246.1.

Mugnai, A., E. A. Smith, and G. J. Tripoli, 1993: Foundations for Statistical-Physical Precipitation Retrieval from Passive Microwave Satellite Measurements. Part II: Emission-Source and Generalized Weighting-Function Properties of a Time-dependent Cloud-Radiation Model. *Journal of Applied Meteorology*, **32 (6)**, 17–39, doi:10.1175/1520-0450(1993)032⟨0017:FFSPRF⟩2.0.CO;2.

Olson, W. S., C. D. Kummerow, G. M. Heymsfield, and L. Giglio, 1996: A Method for Combined Passive-Active Microwave Retrievals of Cloud and Precipitation Profiles. *Journal of Applied Meteorology*, **35 (10)**, 1763–1789, doi:10.1175/1520-0450(1996)035⟨1763:AMFCPM⟩2.0.CO;2.

Olson, W. S., C. D. Kummerow, Y. Hong, and W.-K. Tao, 1999: Atmospheric Latent Heating Distributions in the Tropics Derived from Satellite Passive Microwave Radiometer Measurements. *Journal of Applied Meteorology*, **38 (6)**, 633–664, doi:10.1175/1520-0450(1999)038⟨0633:ALHDIT⟩2.0.CO;2.

Reed, R. J. and E. E. Recker, 1971: Structure and Properties of Synoptic-Scale Wave Disturbances in the Equatorial Western Pacific. *Journal of the Atmospheric Sciences*, **28 (7)**, 1117–1133, doi:10.1175/1520-0469(1971)028⟨1117:SAPOSS⟩2.0.CO;2.

Riehl, H. and J. S. Malkus, 1958: On the heat balance in the equatorial trough zone. *Geophysica*, **6**, 503–538.

Rodgers, C. D., 2000: *Inverse Methods for Atmospheric Sounding: Theory and Practice*. World Scientific, 238 pp.

Saleeby, S. M., S. R. Herbener, S. C. van den Heever, and T. S. L'Ecuyer, 2014: Impacts of cloud nucleating aerosols on shallow tropical convection. *Journal of the Atmospheric Sciences*, In review.

Satoh, S. and A. Noda, 2001: Retrieval of latent heating profiles from TRMM radar data. *Preceedings of the 30th International Conference on Radar Meteorology, Munich, Germany, 19-24 July 2001*, 340–342.

Schumacher, C., P. E. Ciesielski, and M. H. Zhang, 2008: Tropical Cloud Heating Profiles: Analysis from KWAJEX. *Monthly Weather Review*, **136 (11)**, 4289–4300, doi:10.1175/2008MWR2275.1.

Schumacher, C., R. A. Houze, and I. Kraucunas, 2004: The Tropical Dynamical Response to Latent Heating Estimates Derived from the TRMM Precipitation Radar. *Journal of the Atmospheric Sciences*, **61 (12)**, 1341–1358, doi: 10.1175/1520-0469(2004)061⟨1341:TTDRTL⟩2.0.CO;2.

Shannon, C. E. and W. Weaver, 1949: *The Mathematical Theory of Communication, Volume 1*. University of Illinois Press, 117 pp.

Shige, S., Y. N. Takayabu, W.-K. Tao, and D. E. Johnson, 2004: Spectral Retrieval of Latent Heating Profiles from TRMM PR Data. Part I: Development of a Model-Based Algorithm. *Journal of Applied Meteorology*, **43 (8)**, 1095–1113, doi:10.1175/1520-0450(2004)043⟨1095:SROLHP⟩2.0.CO;2.

Simpson, J., R. F. Adler, and G. R. North, 1988: A Proposed Tropical Rainfall Measuring Mission (TRMM) Satellite. *Bulletin of the American Meteorological Society*, **69 (3)**, 278–295, doi:10.1175/1520-0477(1988)069⟨0278:APTRMM⟩2.0.CO;2.

Stephens, G. L., et al., 2008: CloudSat mission: Performance and early science after the first year of operation. *Journal of Geophysical Research*, **113**, D00A18, doi: 10.1029/2008JD009982.

Stevens, B., et al., 2001: Simulations of Trade Wind Cumuli under a Strong Inversion. *Journal of the Atmospheric Sciences*, **58 (14)**, 1870–1891, doi:10.1175/1520-0469(2001)058⟨1870:SOTWCU⟩2.0.CO;2.

Tanelli, S., S. L. Durden, E. Im, K. S. Pak, D. G. Reinke, P. Partain, J. M. Haynes, and R. T. Marchand, 2008: CloudSat's Cloud Profiling Radar After Two Years in Orbit: Performance, Calibration, and Processing. *IEEE Transactions on Geoscience and Remote Sensing*, **46 (11)**, 3560–3573, doi:10.1109/TGRS.2008.2002030.

Tao, W.-K., S. Lang, J. Simpson, and R. Adler, 1993: Retrieval algorithms for estimating the vertical profiles of latent heat release: Their applications for TRMM. *J. Meteor. Soc. Japan*, **71**, 685–700.

Tao, W.-K., et al., 2006: Retrieval of Latent Heating from TRMM Measurements. *Bulletin of the American Meteorological Society*, **87 (11)**, 1555–1572, doi:10.1175/BAMS-87-11-1555.

Twomey, S., 1974: Pollution and the planetary albedo. *Atmospheric Environment (1967)*, **8 (12)**, 1251–1256, doi:10.1016/0004-6981(74)90004-3.

Twomey, S., 1977: The Influence of Pollution on the Shortwave Albedo of Clouds. *Journal of the Atmospheric Sciences*, **34 (7)**, 1149–1152, doi:10.1175/1520-0469(1977)034⟨1149:TIOPOT⟩2.0.CO;2.

van den Heever, S. C., G. G. Carrió, W. R. Cotton, P. J. DeMott, and A. J. Prenni, 2006: Impacts of Nucleating Aerosol on Florida Storms. Part I: Mesoscale Simulations. *Journal of the Atmospheric Sciences*, **63 (7)**, 1752–1775, doi:10.1175/JAS3713.1.

Yanai, M., S. Esbensen, and J.-H. Chu, 1973: Determination of Bulk Properties of Tropical Cloud Clusters from Large-Scale Heat and Moisture Budgets. *Journal of the Atmospheric Sciences*, **30 (4)**, 611–627, doi:10.1175/1520-0469(1973)030⟨0611:DOBPOT⟩2.0.CO;2.

Yang, S. and E. A. Smith, 1999: Moisture Budget Analysis of TOGA COARE Area Using SSM/I-Retrieved Latent Heating and Large-Scale Q 2 Estimates. *Journal of Atmospheric and Oceanic Technology*, **16 (6)**, 633–655, doi:10.1175/1520-0426(1999)016⟨0633:MBAOTC⟩2.0.CO;2.

Zimmerman, J. E., P. J. Smith, and D. R. Smith, 1989: The Role of Latent Heat Release in the Evolution of a Weak Extratropical Cyclone. *Monthly Weather Review*, **117 (5)**, 1039–1057, doi:10.1175/1520-0493(1989)117⟨1039:TROLHR⟩2.0.CO;2.